Inhibitory circuits generate rhythms for leg movements during *Drosophila* grooming

Durafshan Sakeena Syed[1,*], Primoz Ravbar[1], Julie H. Simpson[1,2,*]

[1]Neuroscience Research Institute and Department of Molecular, Cellular and Developmental Biology, University of California, Santa Barbara, Santa Barbara, CA, USA

[2] Lead Contact

*Correspondence: dsakeena@gmail.com (D.S.S.), jhsimpson@ucsb.edu (J.H.S.)

ABSTRACT

Limbs execute diverse actions coordinated by the nervous system through multiple motor programs. The basic architecture of motor neurons that activate muscles which articulate joints for antagonistic flexion and extension movements is conserved from flies to vertebrates. While excitatory premotor circuits are expected to establish sets of leg motor neurons that work together, our study uncovered an instructive role for inhibitory circuits — including their ability to generate rhythmic leg movements. Using electron microscopy data in the *Drosophila* nerve cord, we categorized ~120 GABAergic inhibitory neurons from the 13A and 13B hemilineages into classes based on similarities in morphology and connectivity. By mapping their connections, we uncovered pathways for inhibiting specific groups of motor neurons, disinhibiting antagonistic counterparts, and inducing alternation between flexion and extension. We tested the function of specific inhibitory neurons through optogenetic activation and silencing, using high resolution quantitative analysis of leg movements during grooming. We combined findings from anatomical and behavioral analyses to construct a computational model that can reproduce major aspects of the observed behavior, confirming sufficiency of these premotor inhibitory circuits to generate rhythms.

Keywords: inhibition, motor control, rhythm, premotor, GABA, muscle synergy, limb coordination, connectome

GRAPHICAL ABSTRACT

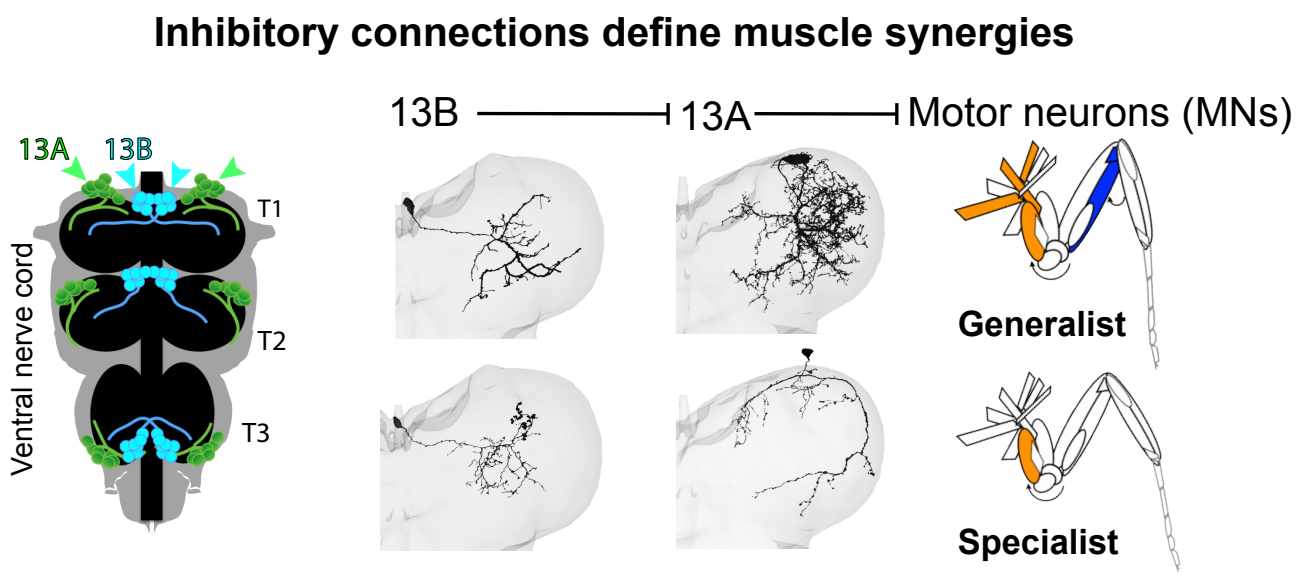

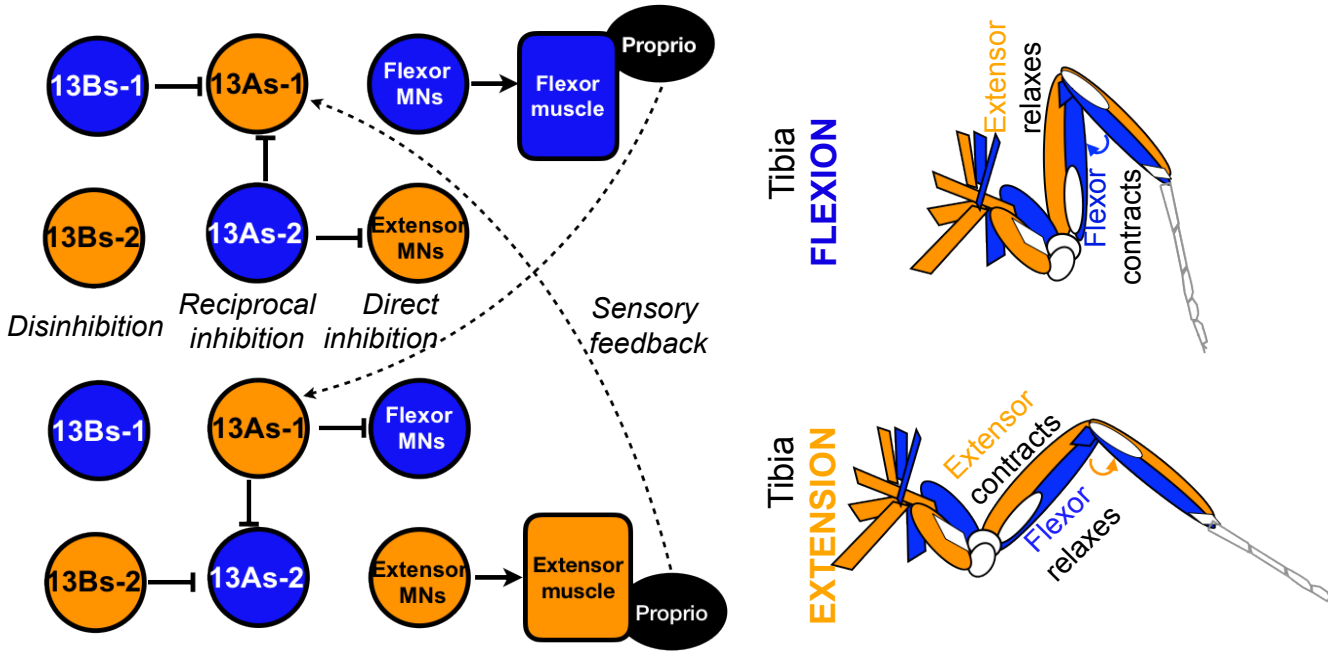

INTRODUCTION

All animals with limbs face the challenge of coordinating their movements to achieve precise motor control. Despite a limited set of muscles in each limb, the nervous system produces multiple flexible actions to generate behavior. These movements rely on a balance of inhibition and excitation, though the specific circuitry remains unclear. *Drosophila* grooming involves coordinated, rhythmic leg movements to sweep the body and remove debris[1] with different actions prioritized sequentially. While sensory, command-like, and motor neurons (MNs) are known components of grooming circuits[2-8], the contribution of GABAergic inhibitory neurons has not been systematically investigated. We hypothesize that these neurons contribute to limb coordination and subroutine selection.

Leg movements during grooming require precise flexor-extensor coordination, controlled by MNs and premotor circuits. Flies use 14 intrinsic leg muscles and 3-5 body wall muscles[9-11], organized into antagonistic pairs. Around 70 excitatory MNs innervate these muscles[11-15,] and recent connectomic mapping has revealed premotor neurons in the ventral cord neuromeres associated with each leg[16,17]. The are around 622 local premotor interneurons[16], suggesting complex control architectures.

We investigate the role of inhibitory neurons in coordinating which leg muscles work together or antagonistically, and how they might produce rhythmic alternations. Neurons from a given lineage usually share a neurotransmitter, and there are 12 GABAergic hemilineages present in the ventral nerve cord (VNC)[18]. We identified neurons from GABAergic 13A and 13B hemilineages in a behavioral screen for grooming defects. Approximately 67±6 13A neurons and 47±1 13B neurons have been reported per hemisegment[18,19]. While activating all 13B neurons induces leg extensions[19], further investigation is required to understand specific role of different subsets in leg coordination. The role of 13A neurons has been unclear due to the lack of exclusive genetic labeling.

Since grooming and walking[20] require leg movements, we expect neural control circuits to overlap, particularly in flexion-extension alternation. MNs controlling similar muscles within a joint receive similar premotor inputs[16]. Descending neurons hypothesized to be involved in walking synapse onto premotor inhibitory neurons from several lineages[17]. These central circuits also receive sensory feedback from leg proprioceptors[21-24]. Recent connectome mapping and genetic tools provide opportunities to test how central and peripheral signals coordinate limb movement.

Muscle synergies describe groups of co-activated muscles, while motor primitives are elemental movement patterns that serve as building blocks of behavior[25-26]. Micro-stimulation of specific spinal cord regions in vertebrate models induced coordinated muscle contractions[27-33], with co-stimulation leading to combinations of contractions, indicating how coordinated regulation by premotor circuits can simplify assembly of more complex movements[26,33-36]. Additional evidence for synergies comes from electromyography, kinematics, neural recordings and computational modeling[37-51]. In

vertebrates, the neural circuits responsible for the coordinated limb movements include motor pools, a topographic map, and commissural neurons[13,14,52-64].The activation of muscles controlling multiple joints (synergies) have been primarily described in terms of excitation[26-33].

We hypothesize that similar synergies could simplify control of the rhythmic leg movements during grooming in flies and that inhibitory circuits play a critical role. We find that inhibitory neurons target different groups of MNs, providing an alternative way to construct muscle synergies. We demonstrate that normal activity of these inhibitory neurons is essential for the rhythmic coordination of leg flexion and extension during grooming. Disrupting inhibitory receptors on MNs in flies reduces locomotion speed[64], but the specific inhibitory neurons involved remain unidentified. By analyzing limb kinematics in grooming flies and silencing specific 13A and 13B neurons, we demonstrate their critical role in spatial and temporal limb coordination. Our findings suggest inhibitory circuits play a broader role in coordinated and rhythmic limb movements.

RESULTS

We describe how inhibitory 13A and 13B neurons affect grooming. We categorize them by morphology, and map their connectivity patterns. We present evidence for muscle synergies and a role of 13A/B neurons in coordinating rhythmic limb movements. Finally, we generate a computational model to integrate and simulate our findings.

Inhibitory Interneurons in 13A and 13B Hemilineages Affect Grooming Behavior

Broad activation of inhibitory neurons causes freezing, while optogenetic activation of fewer neurons in the hemilineages 13A and 13B results in reduced grooming behavior and poor leg coordination, including static over-extension of front legs in clean or dusted flies (Figures 1D, 1F and 1F', Figure 1—Video 1). We conclude that the critical neurons are located in the ventral cord because most Split GAL4 lines only express in the VNC (lack brain expression) (Figure 1—figure supplement 1) and decapitated flies show similar leg extension phenotypes.

Conversely, silencing these neurons locks the front legs in flexion (Figures 1E and 1E', Figure 1—Video 1). Thus, activation or silencing of inhibitory neurons interferes with the alternation of flexion and extension required for dust removal and reduces grooming.

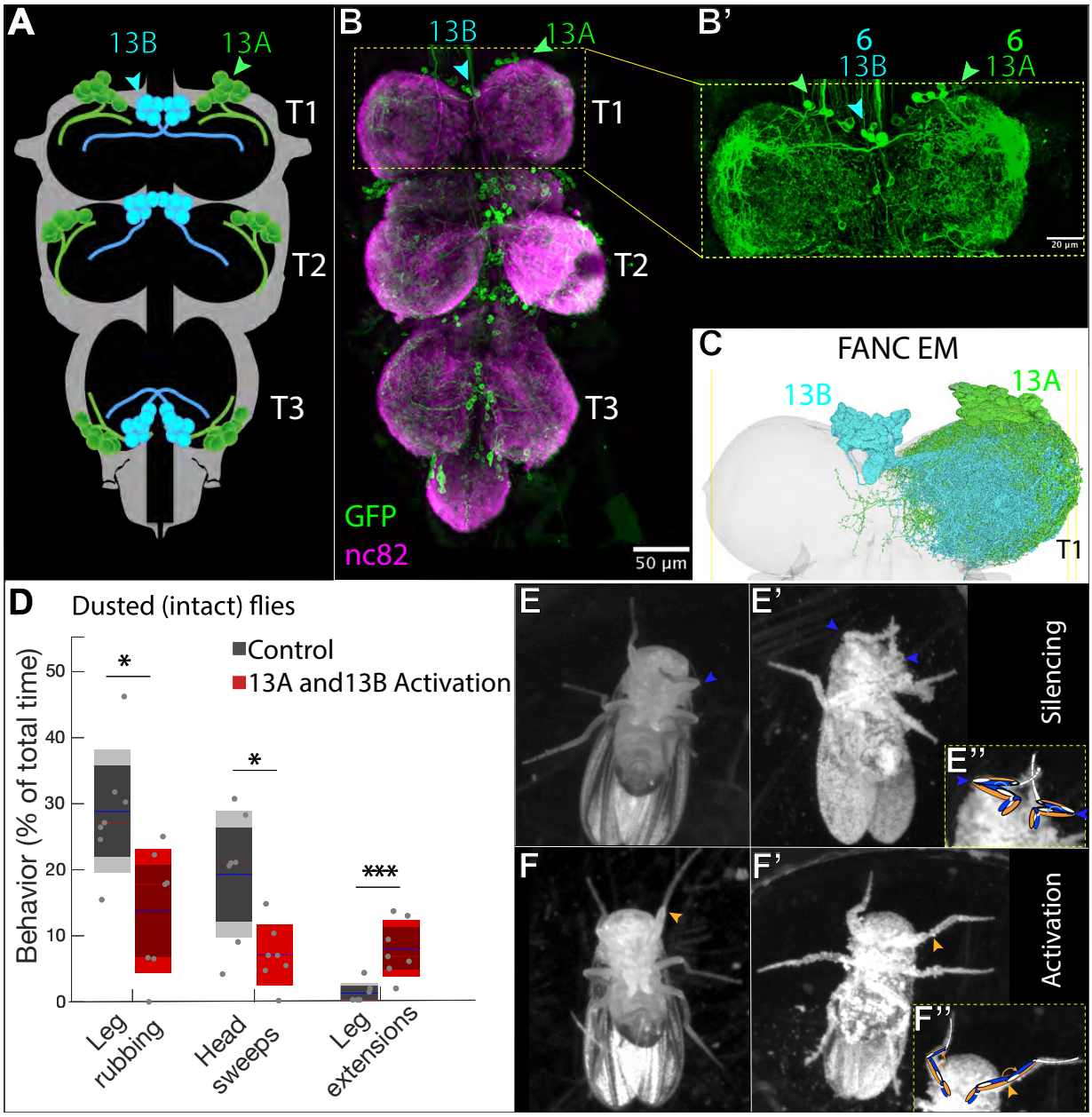

Figure 1. Anatomical Distribution and Behavioral Contributions of 13A and 13B Hemilineages

(A) Schematic showing segmental distribution of 13A (green) and 13B (cyan) neurons across pro-, meta-, and meso-thoracic segments (T1, T2, T3) of VNC.

(B) Confocal image: Six GABAergic 13A neurons (green arrowheads) and six 13B neurons (cyan arrowheads) in each VNC hemisegment, labeled with GFP (green) driven by *R35G04-GAL4-DBD, GAD-GAL4-AD*. Neuropil in magenta (nc82). Panel B' provides a zoomed-in view of T1 region.

(C) EM reconstructions: 62 13A neurons (green) and 64 13B neurons (cyan) in right T1. Ventral side up.

(D) Continuous activation of 13A and 13B neurons labeled by *R35G04-GAL4-DBD, GAD-GAL4-AD* in dusted flies, results in reduced front leg rubbing and head sweeps, and unusual leg extensions (N=7, total time = 4 min).

(E, E') Silencing 13A and 13B neuron subsets (panel B) (R35G04-GAL4-DBD, GAD-GAL4-AD > UAS TNTe) locks one or both front legs in flexion (blue arrowhead) in clean (E) (n=5) and dusted (E') (n=13) headless flies. Panel E" provides zoomed-in view of front legs with a schematic illustrating leg flexion.

(F, F') Activating 13A and 13B neuron subsets (*R35G04-GAL4-DBD, GAD-GAL4-AD > UAS CsChrimson)* induces front leg extension (orange arrowhead) in both clean (F) (n=5), and dusted (F') (n=10) headless flies. Panel F" provides zoomed-in view of front legs with a schematic illustrating leg extension. Also see Figure 1—Video 1.

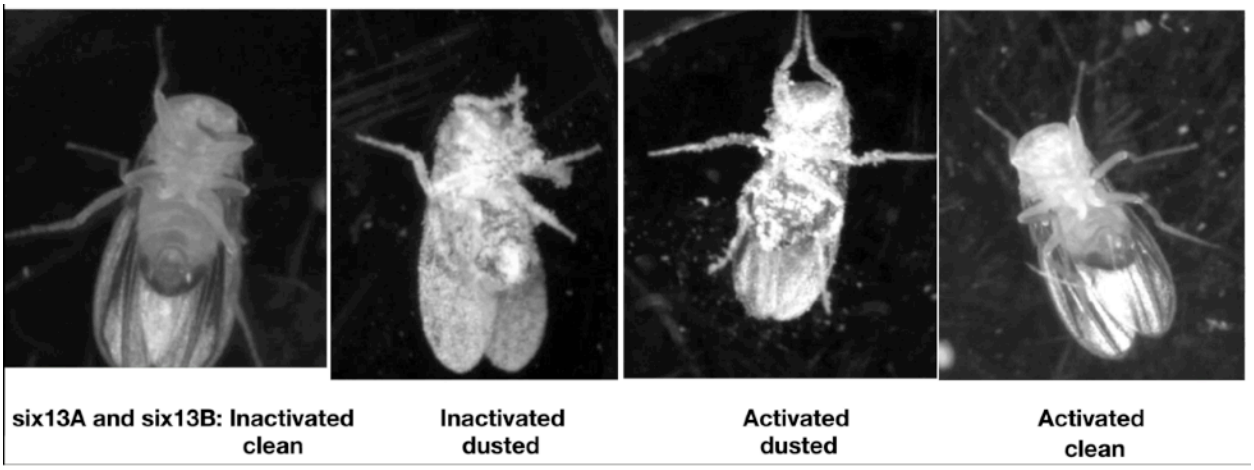

Figure 1—Video 1. Manipulating activity of six 13A neurons and six 13A neurons in headless flies. Inactivation: Legs locked in flexion in clean and dust covered flies. Activation: legs extended in clean and dust covered flies.

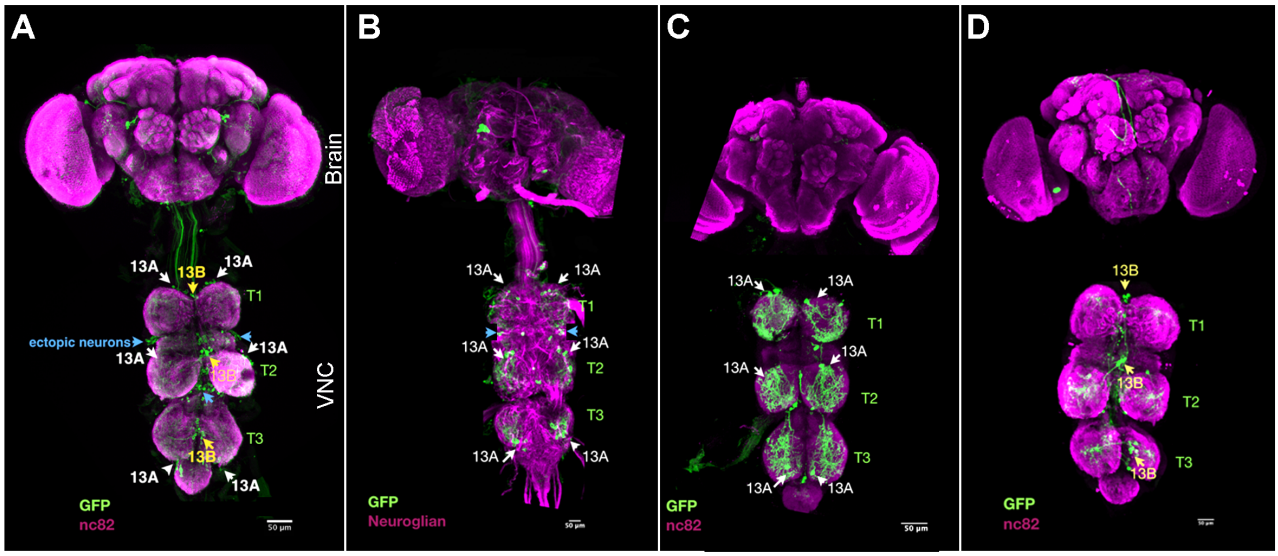

Figure 1—figure supplement 1. Expression pattern in the central nervous system of various lines used for behavior experiments

(A) R35G04-DBD and GAD1-AD Split GAL4 combination labels approximately 6-7 13A neurons and 3 13B neurons per thoracic hemisegment. Ectopic expression is observed in a few neurons in the brain, and in the ventral nerve cord (VNC) in about 9 neurons per hemisegment (possibly 13A neurons with posterior cell bodies or 3B neurons) and 4 neurons per hemisegment (possibly 0A) within the Accessory Mesothoracic neuropil (AMNp) and T2 midline.

(B) R35G04-DBD and Dbx-AD Split GAL4 combination specifically labels a subset of 13A neurons already included in the R35G04-DBD and GAD1-AD Split GAL4 line, thereby isolating 13A neurons without labeling 13B neurons. It also labels approximately 3 neurons per hemisegment with posterior cell bodies and shows no ectopic expression in the brain.

(C) R11C07 and Dbx-AD Split GAL4 combination labels another distinct subset of 13A neurons, with no ectopic expression in the brain.

(D) R11B07-DBD and GAD1-AD Split GAL4 combination labels three 13B neurons. It occasionally labels two ectopic ascending neurons per hemisegment.

Spatial Mapping and Connectivity Patterns of Premotor 13A Neurons in Leg Motor Control

The *Drosophila* nervous system develops from neuroblasts, each of which produces two hemilineages. These lineages arise from neuroblasts that divide briefly embryonically to produce primary neurons and later generate secondary neurons post-embryonically[18,19,65-66]. We focus on the 13A and 13B hemilineages, as manipulating their activity affects grooming. Using serial section electron microscopy dataset[15,] we identified 62 13A neurons and 64 13B neurons in the right front leg neuromere (T1-R) of VNC. Upon entering the neuropil, 13A bundle divides into three sub-bundles, with five large neurons having extensive arbors, primarily in the ventral first sub-bundle of T1-R (Figure 2—video 1). Based on size, location, and connections, we hypothesize these represent early-born primary 13A neurons. We also identified them in the left hemisegment distributed across three sub-bundles.

Lineages contain neurons with distinct shapes and functions. We used NBLAST[72], a computational tool designed to cluster neurons based on morphological similarities, to categorize 13A and 13B neurons into distinct clusters (Figure 2A, Figure 2—figure supplement 3, Figure 2—video 2). Connectivity patterns were analyzed using automatic synapse detection algorithms[11]. While 13A neurons have many post-synaptic partners, their primary targets are MNs (Figure 2—figure supplement 4 and Figure 2—figure supplement 5). Each morphological 13A cluster connects to distinct sets of MNs. Clustering by MN connections correlated with NBLAST morphological clusters, as demonstrated by a cosine similarity matrix (Figure 2 and Figure 2—figure supplement 1). This suggests a spatial map of 13A neurons corresponding to their premotor function. While morphological and connectivity based clusters align, exceptions include cluster 9 and the 13A-3g, which have more diverse connections (Figure 2B and Figure 2—figure supplement 1 B6, H1-H9). Our initial analysis used 13A neurons in the right front leg neuromere (T1R). Comparison to a similar set on the left[16] revealed similar numbers of neurons and cluster divisions (Figure 2—figure supplement 2).

Anatomical features of 13A types suggest possible functional organization. Their dendrites occupy a limited region of VNC, suggesting common pre-synaptic inputs. Axons of 13A neurons overlap with MN dendrites (Figures 2C and 2D, Figure 2—video 3), which are spatially segregated by the leg muscles they innervate, forming a myotopic map[13,14].

Some 13A neurons connect to multiple MNs across various leg segments; others target only a few. We classify these as ‘generalists’ or ‘specialists’. We propose that the broadly projecting primary neurons are generalists, likely born earlier, while specialists are mostly later-born secondary neurons. Four primary 13A neurons (13A-10f-α, -9d-γ, -10g-β, and -10e-δ) are generalists (Figure 2—figure supplement 1 I5-I8 and I9). Secondary neurons in clusters 1, 2, 4, 5, and 7 neurons are specialists, while clusters 6, 8 and 10 are generalists. Clusters 3 and 9 contain a mix. Generalist inhibitory neurons, which target specific MN groups across multiple leg segments could create synergies—coordinated group of muscles that work together.

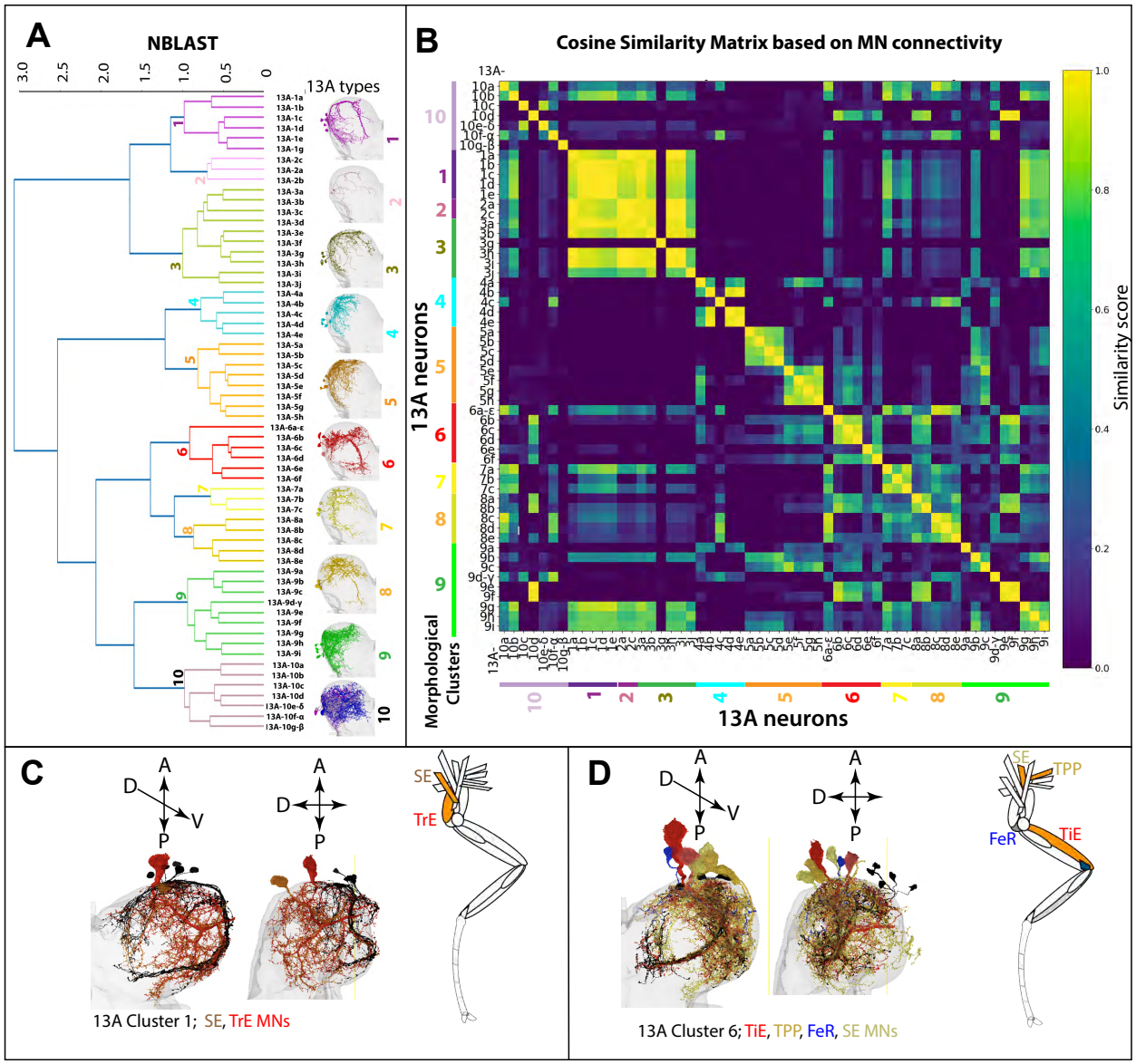

Figure 2. Spatial Map of Premotor 13A Neurons Correlates With Their Connections to Motor Neurons (MNs)

(A) Hierarchical Clustering of 13A Hemilineage. Clustering of 13A neuron types in the right T1 segment was performed using NBLAST, resulting in identification of 10 morphological groups or Clusters. Neurons are named based on morphological clustering. For example, all neurons in the 13A-3 cluster have similar morphology, with 10 neurons labeled as 13A-3 (a-j) (olive). Images of each 13A neuron are shown in Figure 2—Figure Supplement 1. Also see Figure 2—Video 2.

(B) **Cosine similarity graph showing pairwise similarity between 13A neurons based on their MN connectivity patterns.** 13A neurons are organized based on

anatomical clusters obtained with NBLAST as described above. It depicts a correlation between anatomy of 13A neurons and their connections to MNs. For example, 13A-1a, -1b, -1c, -1d (cluster 1) connect to same set of MNs, therefore have high cosine similarity with each other (as seen across the diagonal). Graph also gives insights into groups of 13As that control similar muscles. For example, cluster 1 neurons have high cosine similarity with cluster 3 13A neurons (while, 3g neuron is an exception).

(C, D) **Morphologies of 13A cluster and downstream MNs:** Examples of 13A neuron types classified using NBLAST, alongside their downstream MNs. Neurons within same cluster have similar anatomy, closely positioned within the VNC, with dendrites and axons occupying similar spatial regions. EM reconstructions of two distinct 13A clusters in T1-R are shown. The spatial positions of 13A axons tile the leg neuropil and correspond to the dendrites of MNs they synapse onto. 13A clusters are in black, MNs: extensors (red and brown), flexors (blue). MNs with highest number of synapses are highlighted in red. A= anterior, P= posterior, D= dorsal, V= ventral. Left side depicts a ventral side up, while right side shows ventral toward the right.

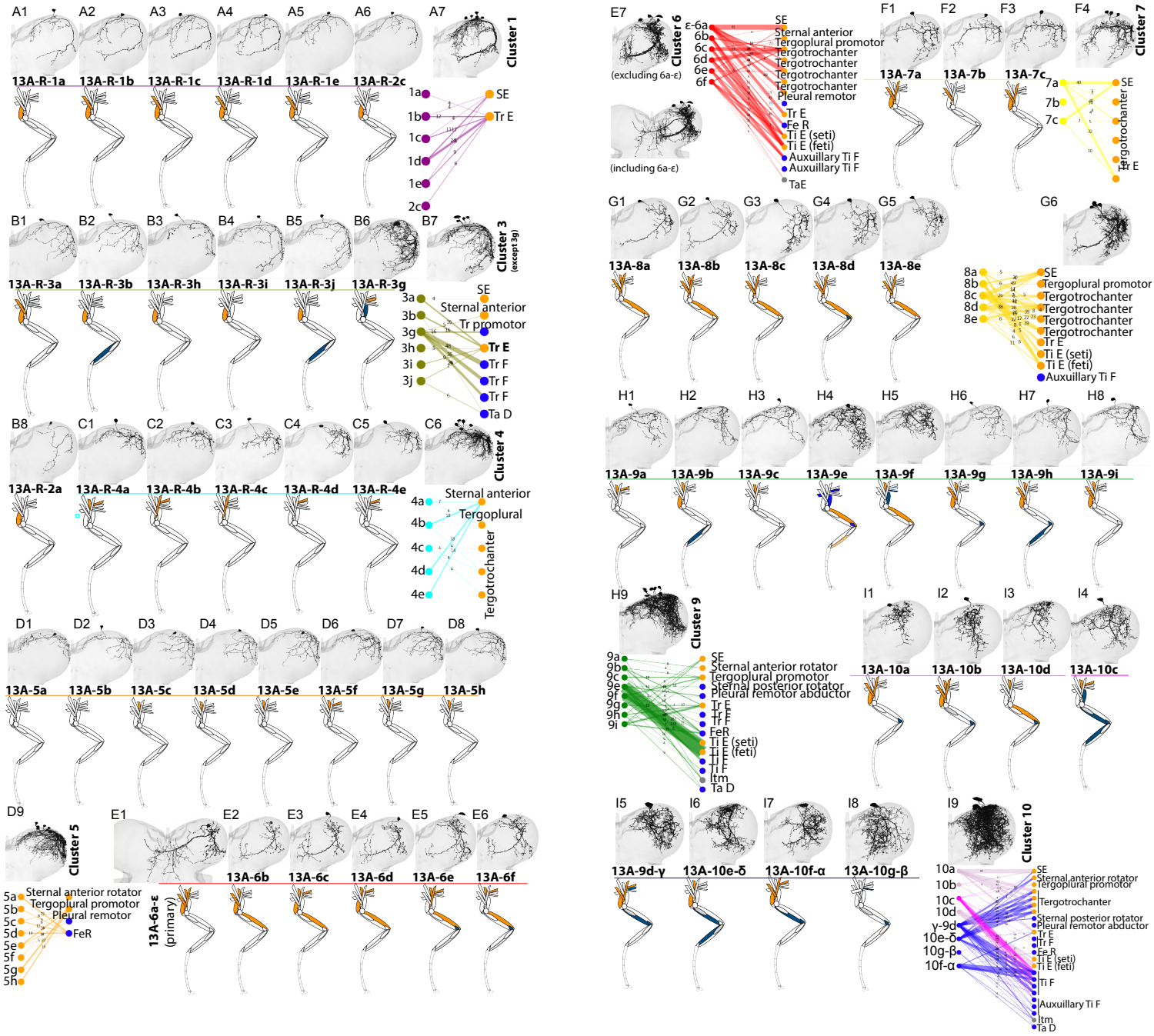

Figure 2—figure supplement 1. Spatial Map and Connectivity of Premotor 13A Neurons

(A1-A6) Top: EM reconstruction showing morphology of individual 13A neurons in cluster-1 in the right hemisegment of prothoracic ganglion (T1) region of VNC. Bottom: Leg schematic illustrating muscles innervated by the MNs inhibited by Cluster-1 13A neurons.

(A7) Top: EM reconstruction showing morphology of all cluster-1 13A neurons combined. Bottom: Connectivity matrix showing cluster 1 13A neurons and their MN connections. These neurons connect to Sternotrochanter extensor (SE) and trochanter extensor (Tr E) both involved in trochanter extension. Edges represent synaptic weight.

(B1-B6) Top: EM reconstruction showing morphology of individual Cluster-3 13A neurons. Bottom: Leg schematic highlighting muscles innervated by the MNs inhibited by Cluster-3 13A neurons.

(B7) Top: Morphology of Cluster-3 13A neurons combined except 13A-R-3g. Bottom: Connectivity matrix showing connections between cluster-3 13A neurons and MNs. Tr =trochanter, Tr E = trochanter extensor, Tr F = trochanter flexor, Ta D= tarsus depressor.

(B8) Top: Morphology of Cluster-2 13A neuron. Bottom: Leg schematic for muscles innervated by the Cluster-2 13A neuron.

(C1-C5) Top: EM reconstruction showing morphology of individual Cluster-4 13A neurons. Bottom: Leg schematic highlighting muscles innervated by the MNs inhibited by Cluster-4 13A neurons.

(C6) Top: Morphology of Cluster-4 13A neurons combined. Bottom: Connectivity matrix showing connections between cluster-4 13A neurons and MNs.

(D1-D8) Top: EM reconstruction showing morphology of individual Cluster-5 13A neurons. Bottom: Leg schematic highlighting muscles innervated by the MNs inhibited by Cluster-5 13A neurons

(D9) Top: Morphology of Cluster-5 13A neurons combined. Bottom: Connectivity matrix showing connections between cluster-5 13A neurons and MNs. Fe R = femur reductor.

(E1-E6) Top: EM reconstruction showing morphology of individual Cluster-6 13A neurons. Bottom: Leg schematic highlighting muscles innervated by the MNs inhibited by Cluster-6 13A neurons.

(E7) Left: Morphology of Cluster-6 13A neurons combined. Right: Connectivity matrix showing connections between cluster-6 13A neurons and MNs.

(F1-F3) Top: EM reconstruction showing morphology of individual Cluster-7 13A neurons. Bottom: Leg schematic highlighting muscles innervated by the MNs inhibited by Cluster-7 13A neurons.

(F4) Top: Morphology of Cluster-7 13A neurons combined. Bottom: Connectivity matrix showing connections between cluster-7 13A neurons and MNs.

(G1-G5) Top: EM reconstruction showing morphology of individual Cluster-8 13A neurons. Bottom: Leg schematic highlighting muscles innervated by the MNs inhibited by Cluster-8 13A neurons.

(G6) Top: Morphology of Cluster-7 13A neurons combined. Bottom: Connectivity matrix showing connections between cluster-7 13A neurons and MNs.

(H1-H8) Top: EM reconstruction showing morphology of individual Cluster-9 13A neurons. Bottom: Leg schematic highlighting muscles innervated by the MNs inhibited by Cluster-9 13A neurons.

(H9) Top: Morphology of Cluster-9 13A neurons combined. Bottom: Connectivity matrix showing connections between cluster-9 13A neurons and MNs.

(I1-I8) Top: EM reconstruction showing morphology of individual Cluster-10 13A neurons. Bottom: Leg schematic highlighting muscles innervated by the MNs inhibited by Cluster-10 13A neurons.

(I9) Top: Morphology of Cluster-10 13A neurons combined. Bottom: Connectivity matrix showing connections between cluster-10 13A neurons and MNs.

Extensors in orange and Flexors blue.

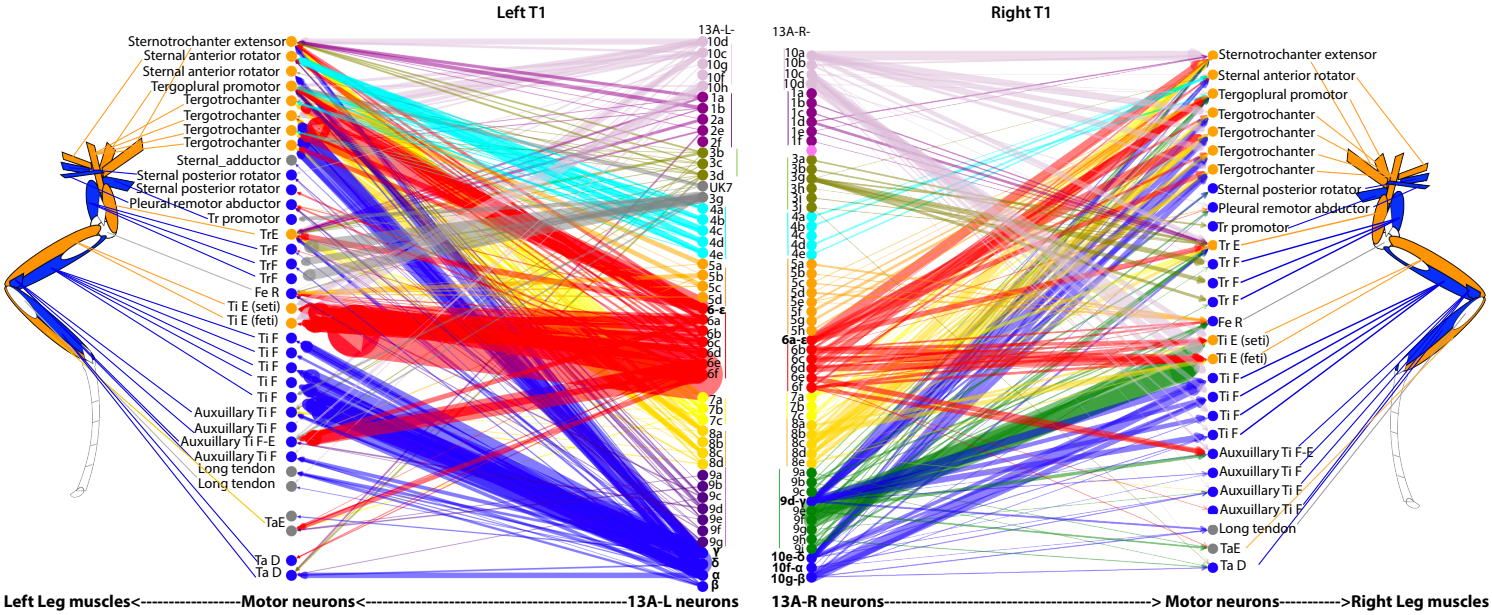

Figure 2—Figure Supplement 2. Connectivity Matrix of 13A Neurons and the Motor Neurons Showing Left-Right Comparison and Spatial Map. The 13A neurons that belong to the same anatomical cluster connect to same set of motor neurons (MNs). 13A neurons that have similar morphology are shown in the same color. Clusters that contain similar neurons on the *right and the left* are shown in one color. The edge width between 13A neurons and motor neurons corresponds to the normalized synaptic weight. Each cluster on the right and the left connects to the same set of MNs. Synaptic weights on the left[15] are greater than on the right, but the connections and preferred partners are the same. The leg schematic shows the muscles that these MNs innervate. Extensor muscles: orange, flexors: blue.

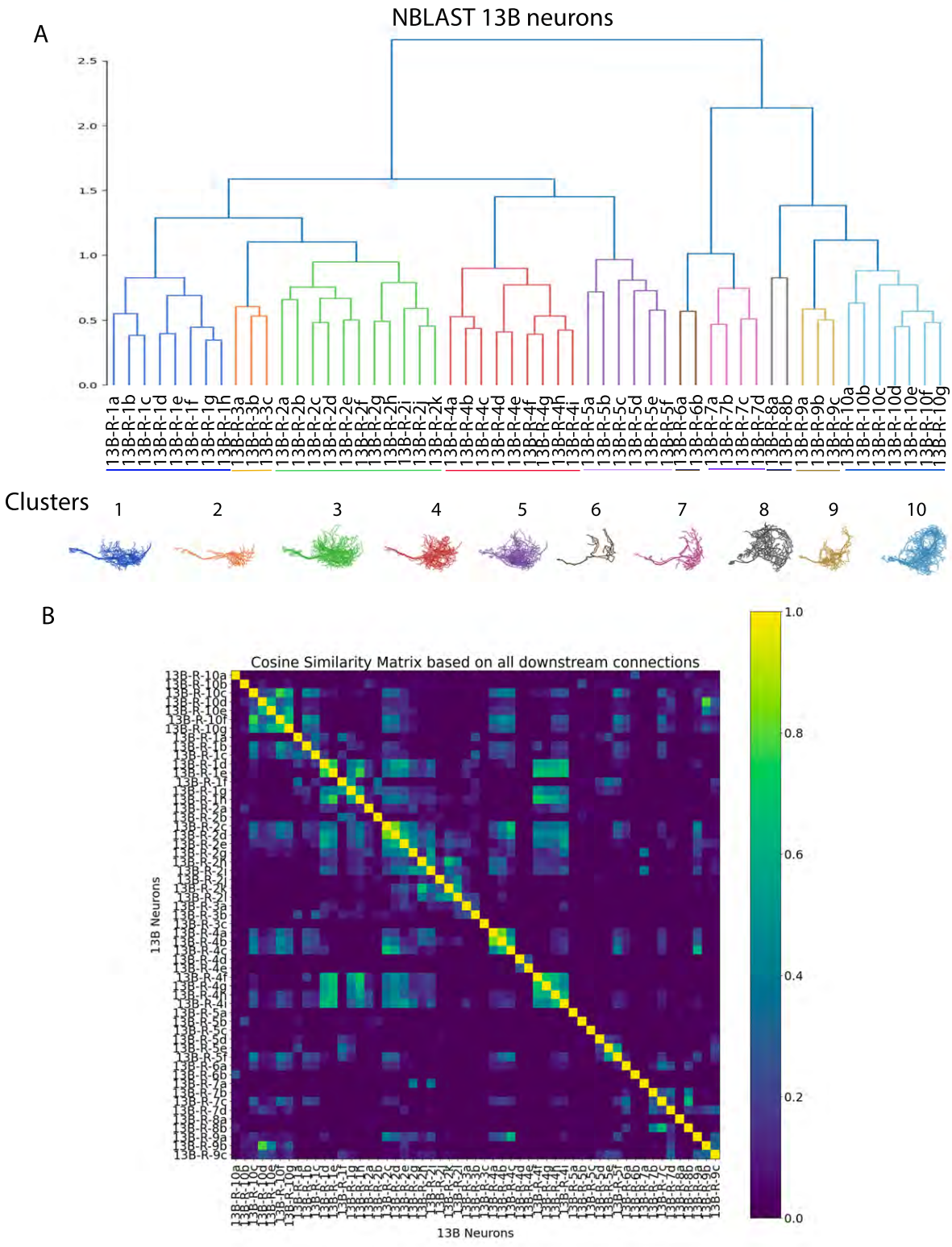

Figure 2—figure supplement 3. Anatomical classification of 13B neurons.

(A) Hierarchical clustering of 13B hemilineage in the right (R) T1 based on NBLAST similarity scores. Each cluster is depicted in a different color. The neurons having

similar morphology represent one cluster. Neurons are named based on morphological clustering, for example, all neurons in the 13B-R-1 series have similar morphology and contain 8 neurons 13B-R-1(a-h). Bottom panel shows visualization of clusters in a 2D space. Each subplot depicts a distinct cluster, with different colors indicating different clusters.

(B) Cosine similarity graph showing the pairwise similarity between 13B neurons based on their connections to all downstream neurons. 13B neurons are named based on the anatomical clusters obtained with NBLAST as described above.

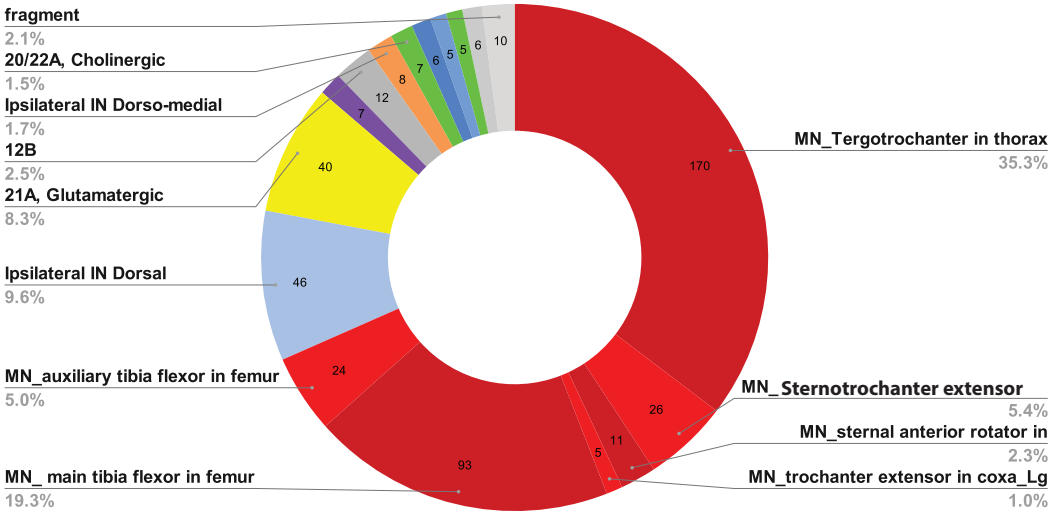

Figure 2—figure supplement 4. Neurons Downstream of a Primary 13A-10f-α Neuron. Motor neurons (red) constitute 58.4% of the total downstream synapses. Other downstream connections include glutamatergic hemilineages, 21A, 24B (yellow), cholinergic hemilineages 7B, 3A, 20A (green), GABAergic hemilineages 12B (gray), and other unknown neurons (blue, orange).

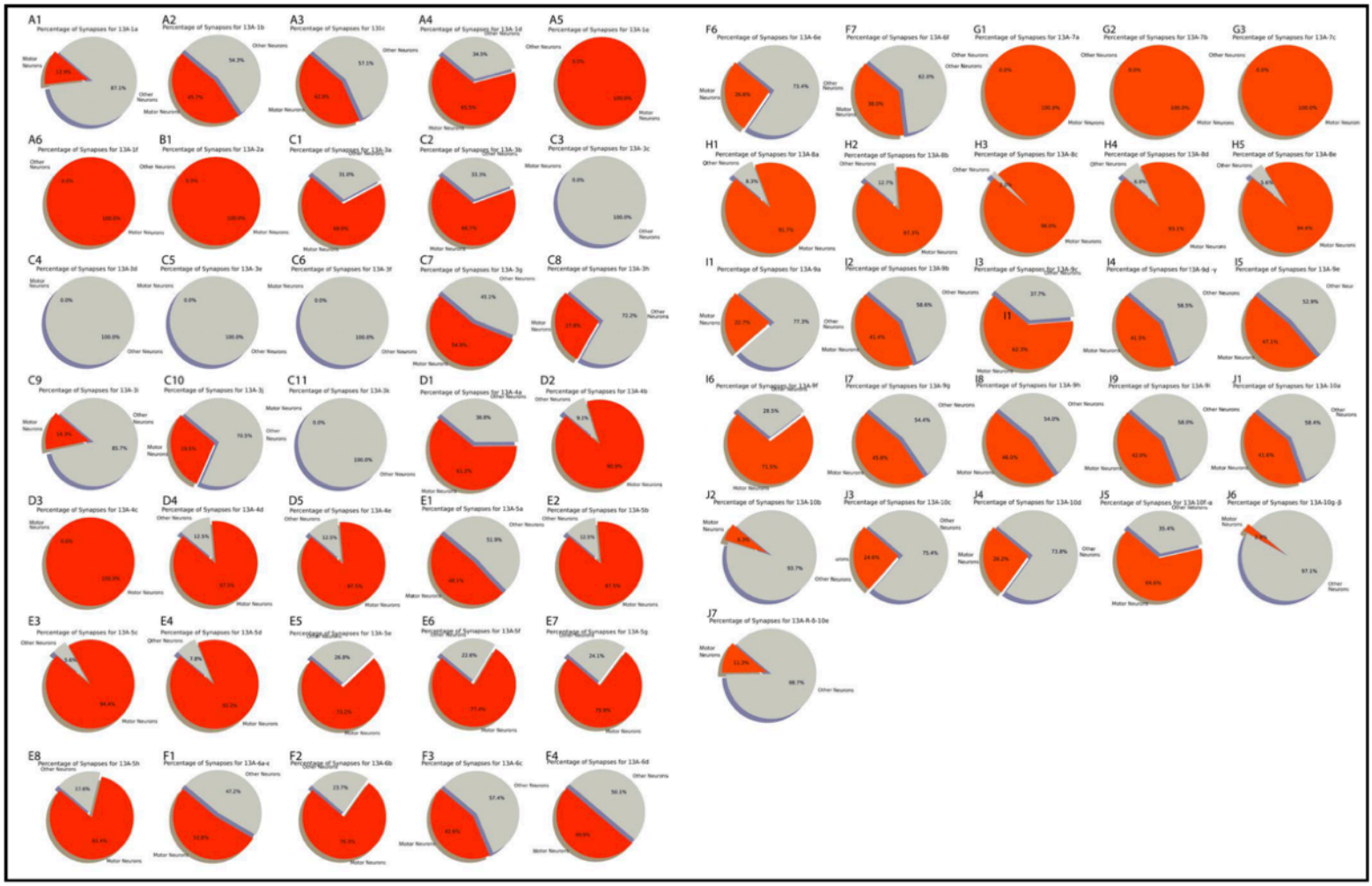

Figure 2—figure supplement 5. Percentage of downstream synapses of 13A neurons that directly connect to motor neurons (MN). MN connections in red and other neurons in gray. (A1-A5) Cluster 1 13A neurons. (B1) Cluster 2 13A neuron. (C1-C11) Cluster 3 13A neurons. (D1-D5) Cluster 4 13A neurons. (E1-E8) Cluster 5 13A neurons. (F1-F7) Cluster 6 13A neurons. (G1-G3) Cluster 7 13A neurons. (H1-H5) Cluster 8 13A neurons. (I1-I9) Cluster 9 13A neurons. (J1-J7) Cluster 10 13A neurons.

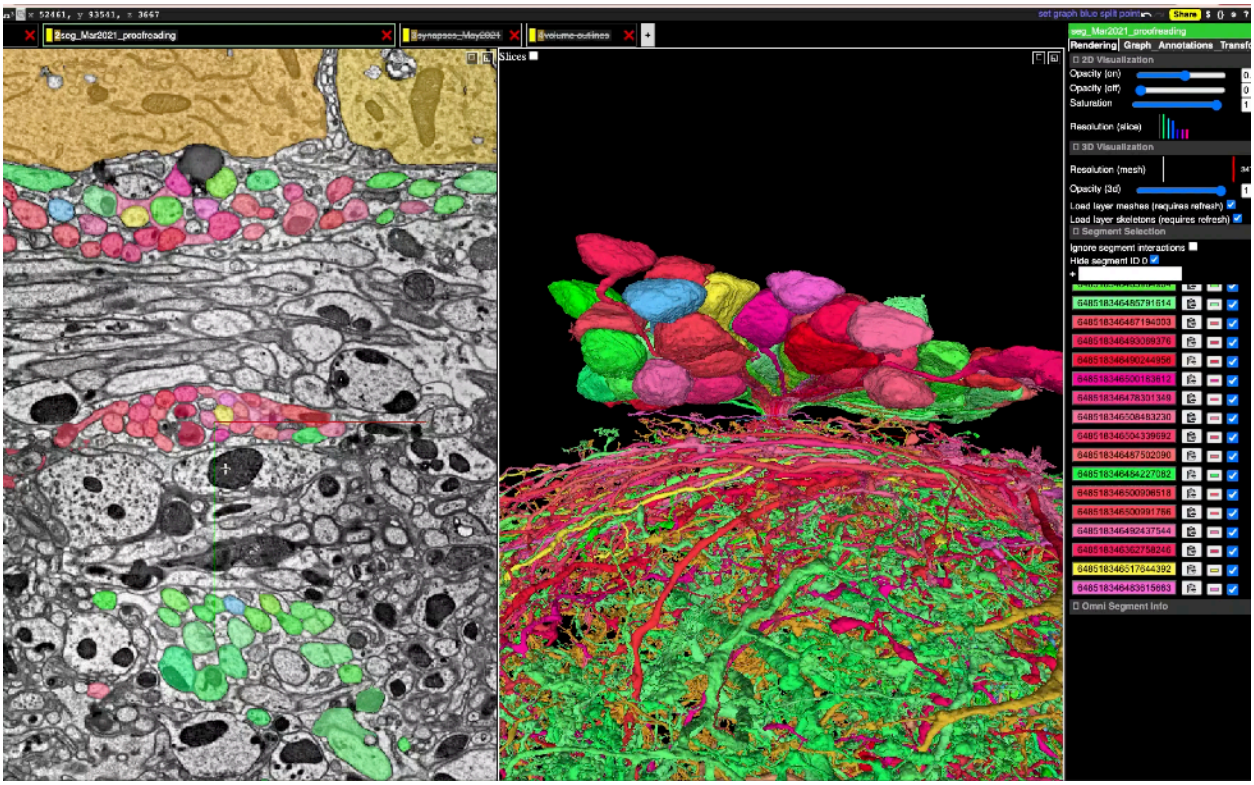

Figure 2—video 1. 13A neurons in the right front leg neuromere (T1R). Primary neurons in brown. Secondary neurons in green and red. Three sub-bundles of hemi-lineage 13A neurons are shown across 2D EM sections (left) and 3D rendering (right) of the cell bodies and 13A axonal tracks entering the neuropil.

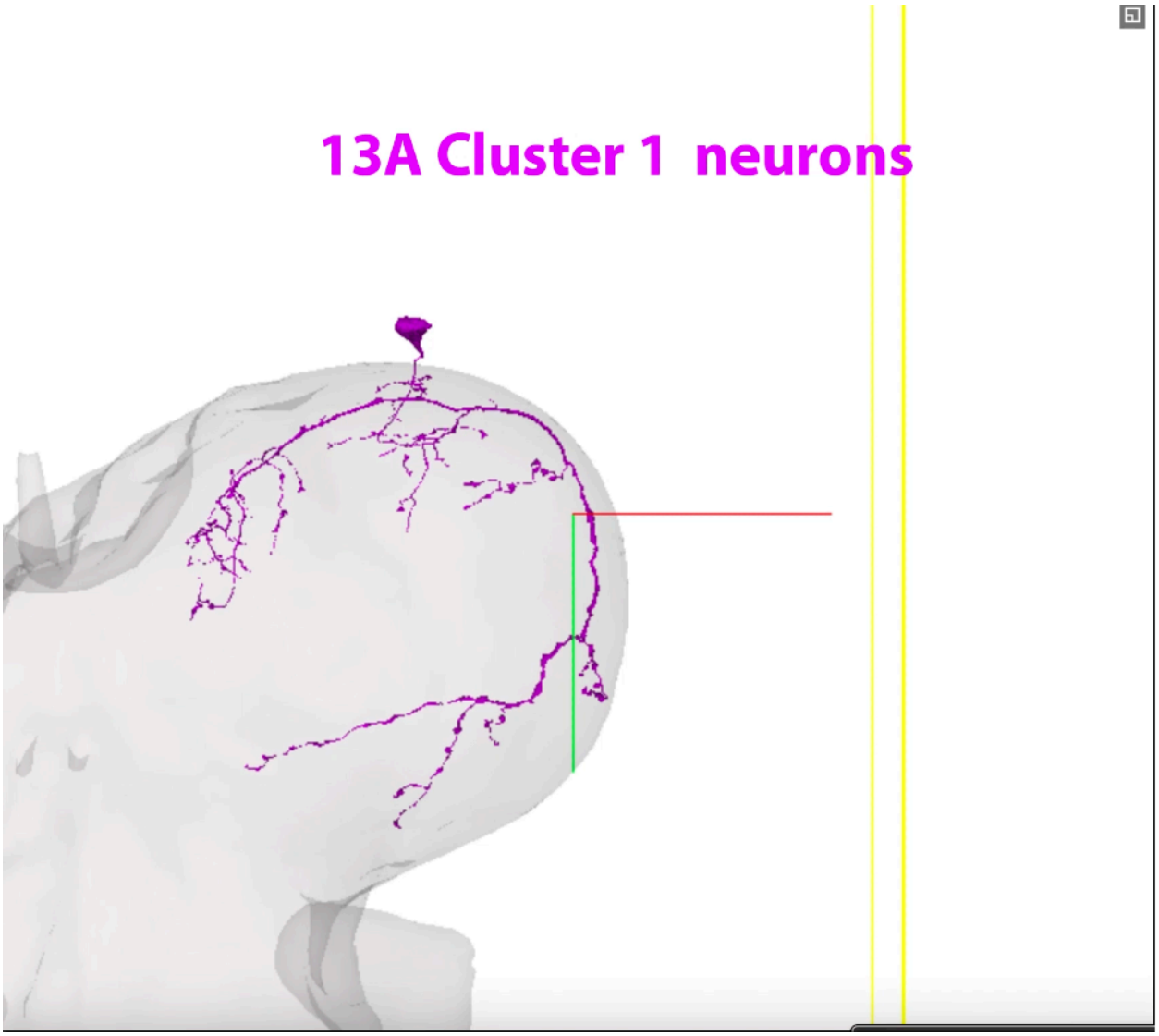

Figure 2—video 2. 13A morphological clusters

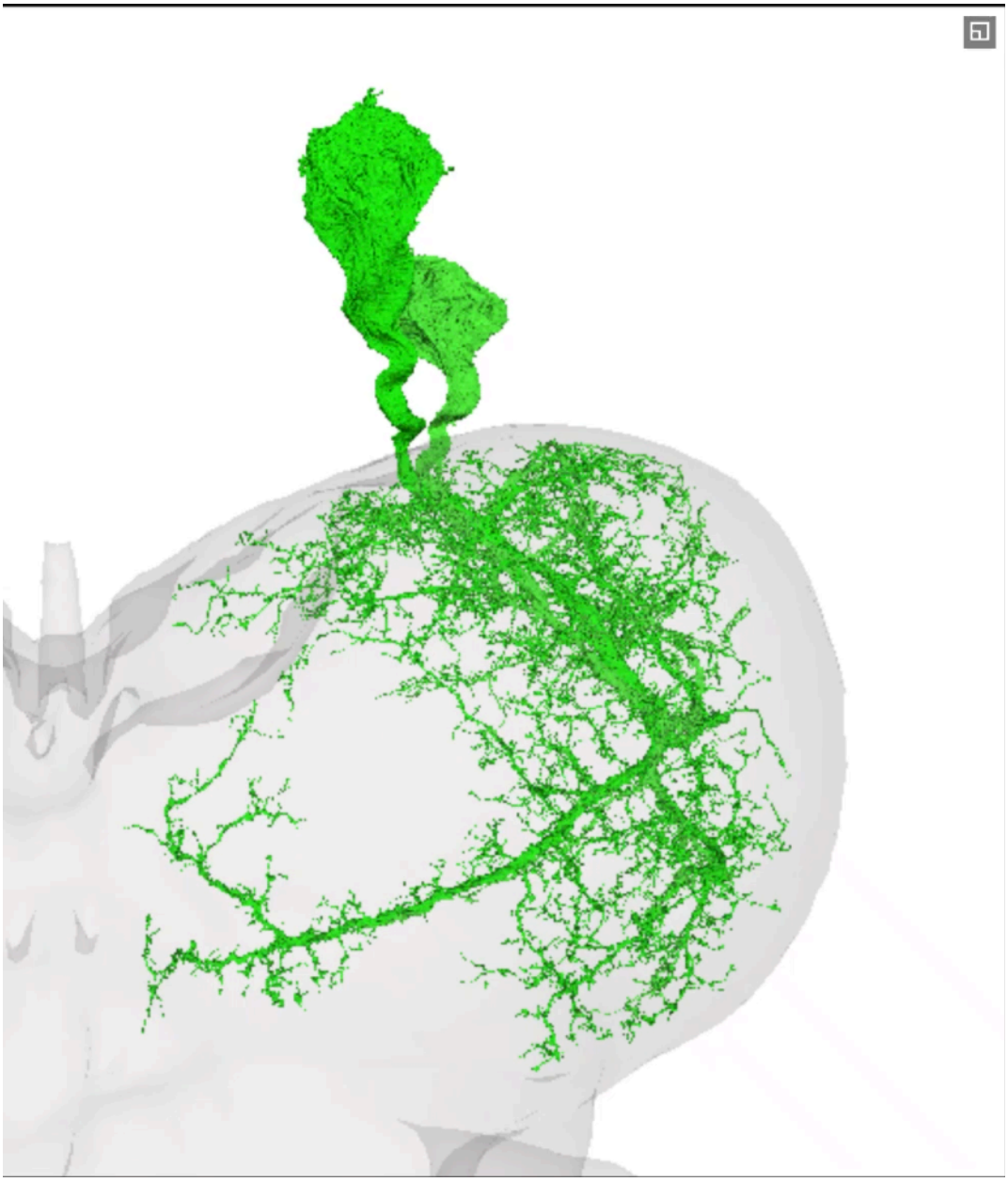

Figure 2—video 3. 13A cluster 6 neurons (red) and downstream Tibia extensor MNs (feti and seti, green)

Connectivity Motifs for Coordinated Control

We analyzed the connectivity of 13A/B neurons synapsing onto MNs of the medial joint (Figure 3). Interconnections between 13A neuron types suggest a role in generating flexor-extensor antagonism. 13A neurons synapsing onto extensor MNs also inhibit 13A neurons targeting flexors, and vice versa (Figures 3A2, 3A3, 3B). These redundant circuits would ensure that at a given time point either extensor or flexor is active.

These 13A groups are also reciprocally connected to each other (Figures 3A4, 3A5, 3B) providing a mechanism for alternation between flexion and extension over time.

This organizational motif applies to multiple joints within a leg as reciprocal connections between generalist 13A neurons suggest a role in coordinating multi-joint movements in synergy (Figure 3C).

We did not find any correlation between the morphology of premotor 13B and motor connections, but there is a topographically restricted output based on their 13A premotor targets (Figure 2—figure supplement 1 and Figure 3—figure supplement 1B). 13B neurons connect to 13A neurons targeting either flexor or extensor MNs (Figure 3—figure supplement 1B and Figure 3—figure supplement 2). Two specific 13B neurons inhibit both extensor MNs and disinhibit flexor MNs, playing a dual role. Twenty-four 13B neurons from clusters 1 to 4 target 13A neurons.

Interconnections between 13A and 13B neurons reveal additional inhibitory motifs that could mediate movement of other joints or multiple joints synergistically. 13B neurons disinhibit MNs by inhibiting premotor 13Bs or 13As. For example, 13B-4h inhibits 13B-2i, a generalist premotor neuron targeting proximal flexor and medial extensor MNs (Figure 3—figure supplement 1 A, E, F), while preventing disinhibition of antagonistic MNs (Figures 3B and Figure 3—figure supplement 1B). Similarly, 13As could disinhibit antagonistic MNs by inhibiting premotor 13Bs. For example, primary 13A-10g-β connects to 16 13B neurons, disinhibiting proximal extensor MNs while inhibiting proximal/medial flexors (Figure 3—figure supplement 1A, D, F)

Together, inhibitory interconnections among 13A neurons, and between 13A and 13B neurons may coordinate the alternating activity in antagonistic muscle groups.

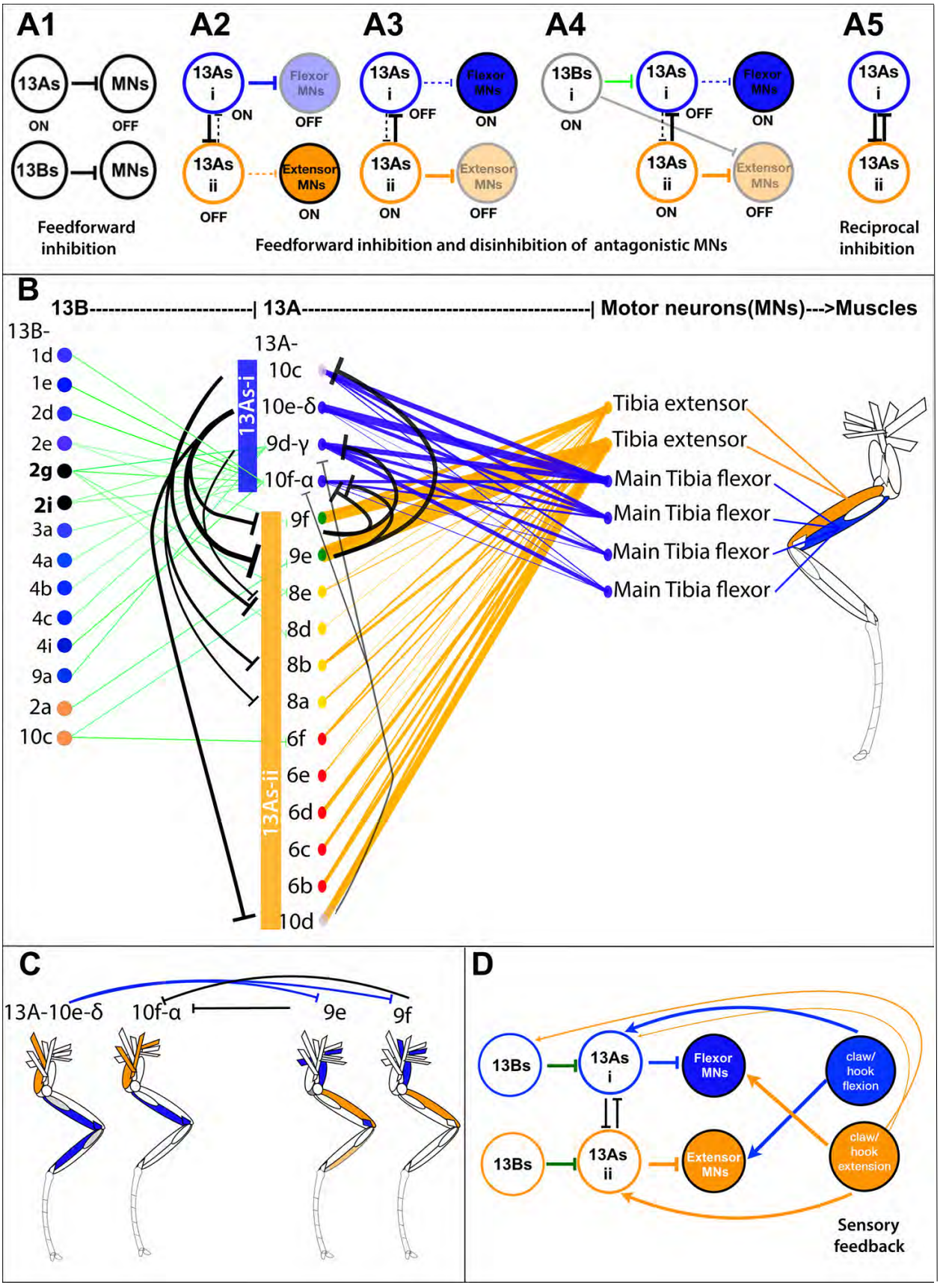

Figure 3. Inhibitory Circuitry for Antagonistic Muscle Control

(A) **Schematic of inhibitory circuit motifs (A1)** Direct MN inhibition by 13A/B neurons. **(A2)** Flexor inhibition and extensor disinhibition: 13As-i inhibit flexor MNs and disinhibit extensor MNs by inhibiting 13As-ii. **(A3)** Extensor inhibition and flexor disinhibition: 13As-ii inhibit extensor MNs and disinhibit flexor MNs by inhibiting 13As-i. **(A4)** 13B mediated disinhibition: 13Bs disinhibit MNs by targeting premotor 13As, while some also directly inhibit antagonistic MNs. (A5) Reciprocal inhibition among 13A groups that inhibit antagonistic MNs may induce flexor-extensor alternation.

(B) **Connectivity matrix:** Inhibitory connections regulating antagonistic MNs of the medial joint. Leg schematic shows tibia extensor (orange) and flexor (blue) muscles, innervated by respective MNs. Flexor-inhibiting 13A neurons (13As-i) in blue, and extensor inhibiting 13As (13As-ii) in orange.

Direct MN inhibition: Primary neurons (13A-10f-α, 9d-γ, and 10e-δ) and 13A-10c (13As-i) connect to tibia flexor MNs (blue edges), making a total of 85, 219, 155, 157 synapses, respectively. Twelve secondary 13As ii inhibit tibia extensor MNs (orange edges), with strong connections from 13A-9f, -9e, and -10d totaling 188, 275, 155 synapses, respectively.

Reciprocal inhibition: Three neurons from 13As-i inhibit six from 13As ii, with 13A-10e-δ connecting to 13A-9f (19 synapses), -9e (31), and -10d (14). 13A-10c connects to 13A-8a (6), -8b (12), and -8e (5). 13A-9d-γ connects to 13A-8e (8). Conversely, three from 13As-ii inhibit two neurons from 13As i, with 13A-9f connecting to 13A-10f-α (25) and -9d-γ (6), and 13A-10d connecting to 13A-10f-α (8), -9d-γ (7), and -10e-δ (15). 13A-9e connects to 13A-10f-α (21) and -10c (47) (black edges).

Disinhibition by 13B neurons: 13B connects to 13As-i (13A-10f-α and -9d-γ) (totaling 78 and 50 synapses) (green edges), disinhibiting flexor MNs. 13B-2g and -2i also directly inhibit tibia extensor MNs.

Reciprocal inhibition for multi-joint coordination: Primary 13As (10e-δ and 10f-α) target proximal extensor MNs and medial/distal flexors, while secondary 13As (9e and 9f) target antagonist muscle groups, indicating generalist 13As coordinate muscle synergies through reciprocal inhibition.

(C) **Proprioceptive feedback:** Sensory feedback from proprioceptors onto reciprocally connected 13As could turn off corresponding MNs and activate antagonistic MNs. Flexion-sensing proprioceptors target extensor MNs and 13As-i that inhibit tibia flexor MNs. Thus, after flexion completion, this feedback could induce extension and inhibit flexion via 13A neurons. Extension-sensing proprioceptors target tibia flexor MNs and two 13As (13As-ii) that inhibit extensor MNs. Claw extension neurons also connect to 13A-δ. 13Bs that disinhibit flexor MNs also receive connections from extension-sensing proprioceptors. Thus, extensor-sensing neurons can initiate flexion by directly activating MNs, disinhibit flexion by activating 13As-ii/13B neurons, and inhibit extension via 13As-ii neurons. Also see Figure 3—figure supplement 3.

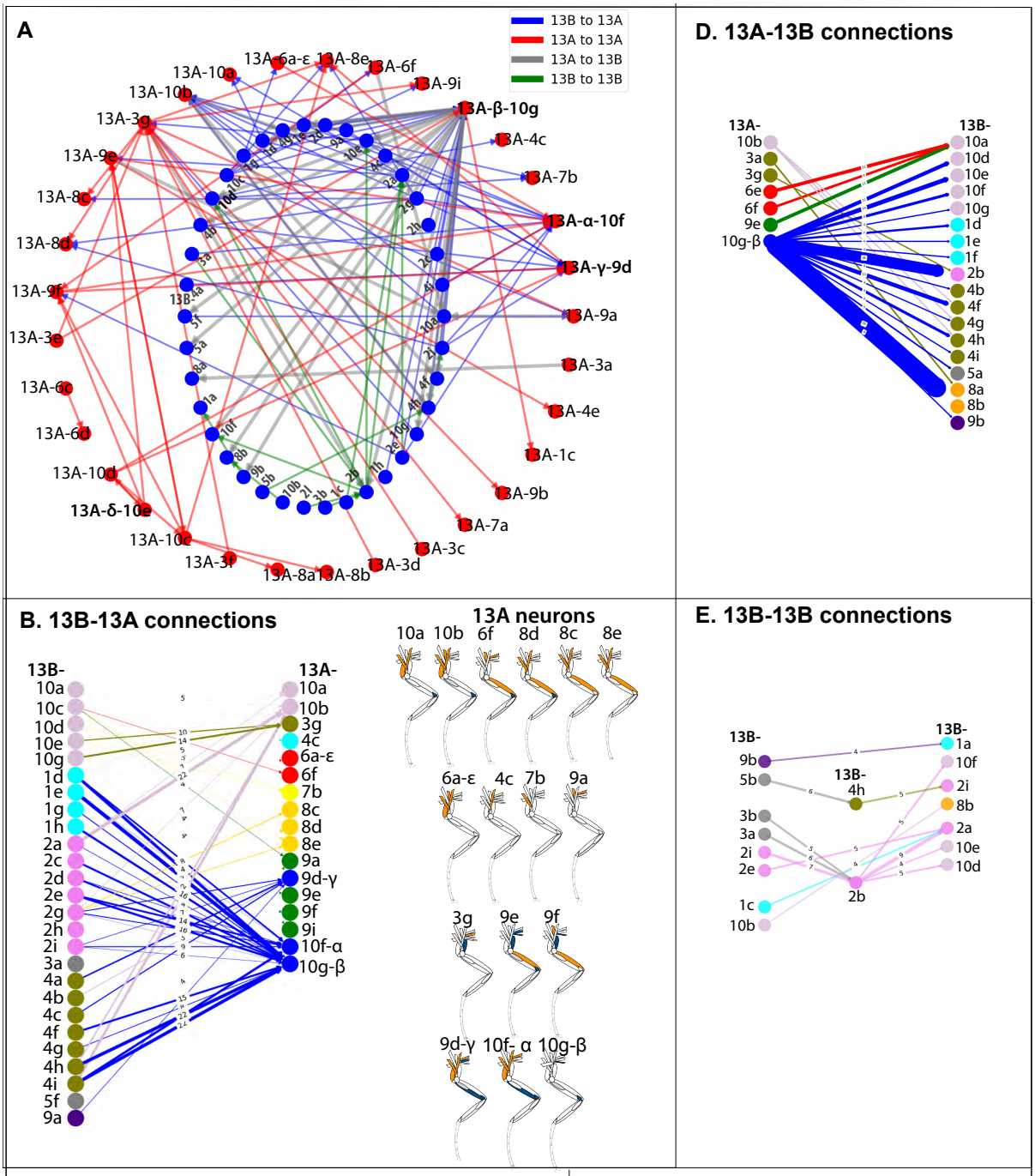

Figure 3—figure supplement 1. Disinhibition Matrix

(A) Network Visualization of all 13A and 13B Neuronal Interconnections. Network graph showing all 13B (presynaptic) to 13A (postsynaptic) connections (blue edges), 13A to 13A connections (red edges), 13A to 13B connections (gray edges) and 13B to 13B connections (green edges). 13A nodes in red. 13B nodes in blue.

(B) Disinhibition mediated by 13B neurons: A connectivity graph showing all 13B to 13A connections.The leg schematic on the right side shows targets of motor neurons inhibited by these 13A neurons, which are disinhibited by 13B neurons. Nodes of the same color within a lineage represent neurons within the same morphological cluster. Edge color corresponds to the postsynaptic 13A targets. Extensors in orange, Flexors in blue.

(C) Disinhibition mediated by 13A-13A connections: A connectivity graph highlighting connections within 13A neurons that leads to disinhibition of motor neurons. Nodes of the same color represent same 13A anatomical cluster. Primary 13A neuron nodes are highlighted in blue, except for 13AR-6a(-ε) that is highlighted in red. Color of the edges corresponding to the color of a presynaptic neuron.

(D) Disinhibition mediated by 13A-13B connections: A connectivity graph showing connections from 13A neurons to 13B neurons. Note that most of these postsynaptic 13B neurons are premotor (shown in panel F).

(E) Disinhibition mediated by 13B-13B connections: A connectivity graph showing interconnections between 13B neurons.

(F) Premotor 13B neurons: A connectivity graph showing premotor 13B neuron connections to MNs. 13B neurons that are morphologically related (same cluster) are shown in same color. 13B neurons that belong to the same cluster do not connect to same set of motor neurons. Extensors in orange, Flexors in blue.

A

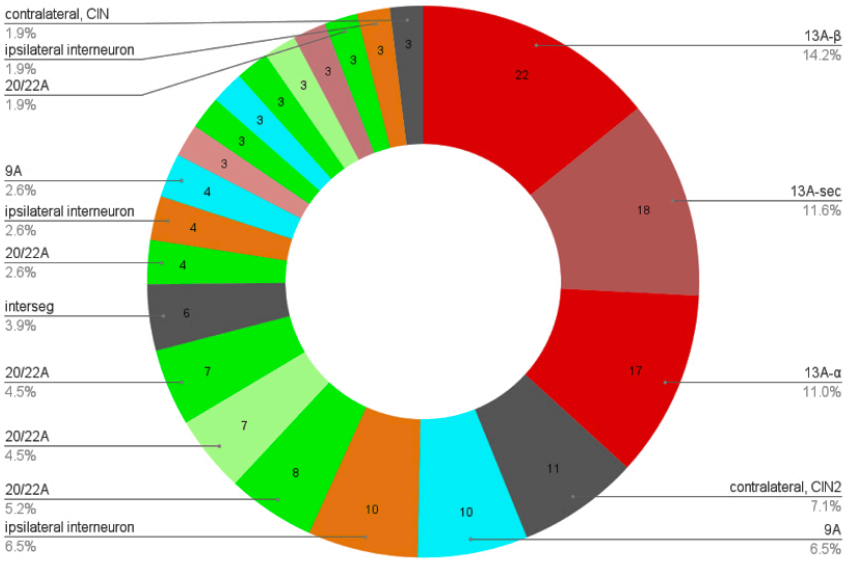

B

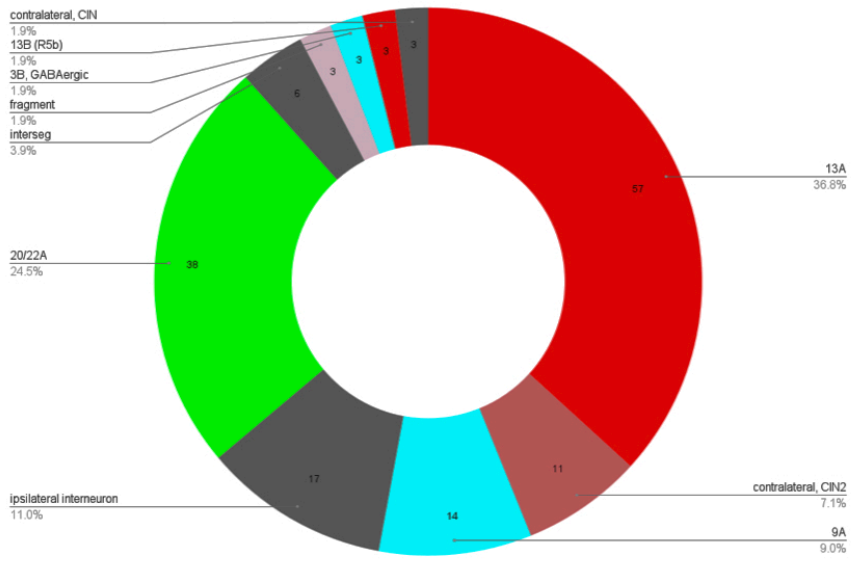

Figure 3—figure supplement 2. Neurons Downstream of a 13B Neuron (13B-4i). 13A neurons (red) comprise 36.8% of the total downstream synapses. 20/22A cholinergic neurons (green), 24.5% of the total synapses. 9A neurons (cyan)(6.5%), two contralateral interneurons (9%), 13B neuron (1.9%), 3B (1.9%), ipsilateral interneurons (possibly 21A?) (11%) of the total downstream partners. A. Individual downstream neurons. B. Aggregate of the same type of neurons.

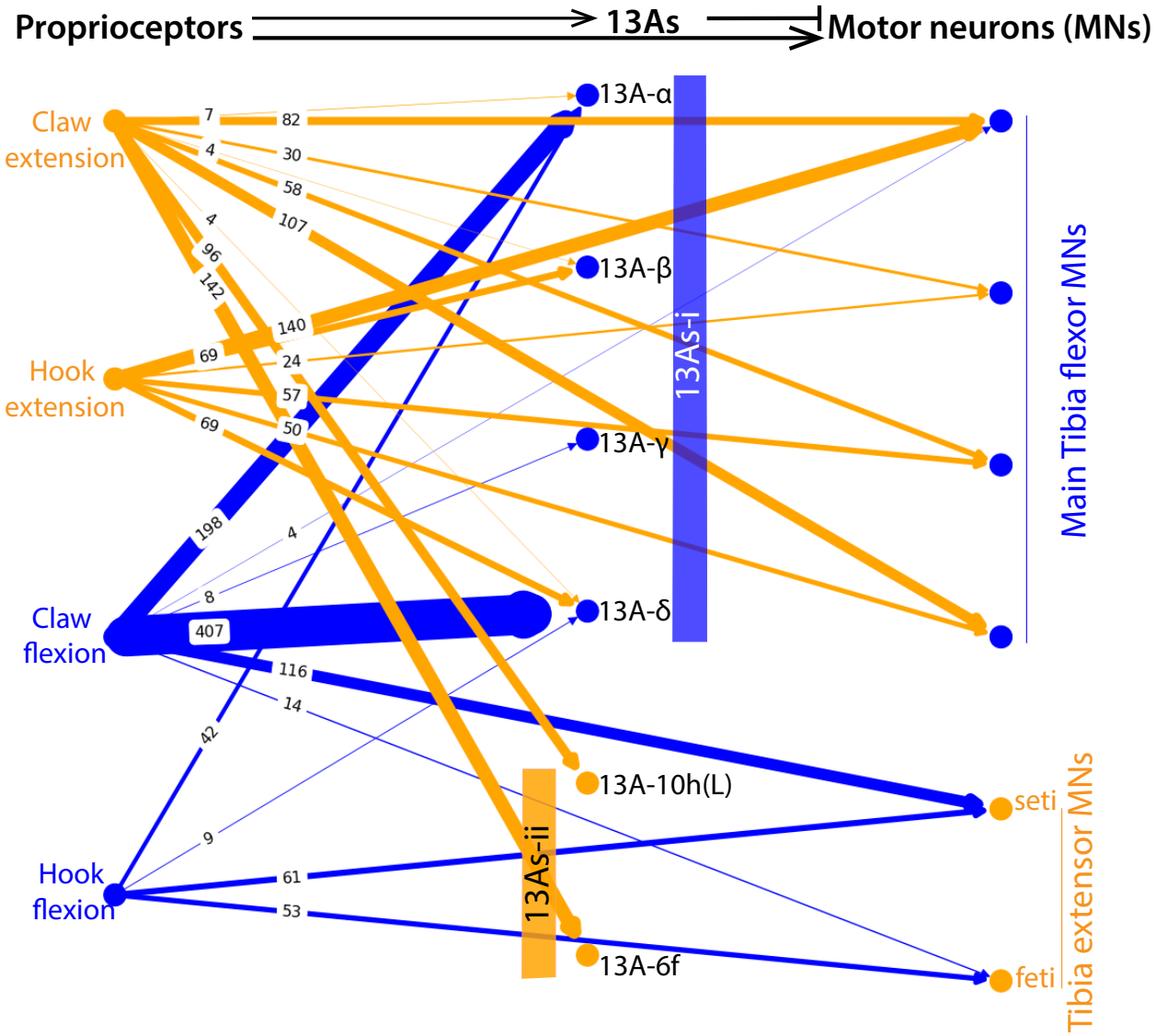

Figure 3—Figure Supplement 3. Sensory Feedback Onto Inhibitory 13A Neurons and Motor Neurons. Connectivity Matrix Showing Position Sensing Claw Neurons and Motion Sensing Hook Neurons Send Feedback Connections to 13A Neurons and Antagonistic MNs. Flexion Position and Motion Sensing Proprioceptors (Blue) Neurons Connect to Tibia Extensor MNs and Primary 13As (13As-I Group) That Inhibit Tibia Flexor MNs. Thus, When the Flexion Is Complete, It Could Induce Extension and Inhibit Flexion Via 13A Neurons. Similarly, Extension Position and Motion Sensing Proprioceptors (Orange) Neurons Connect to Tibia Flexor MNs and Two 13As (13As-Ii Group) That Inhibit Tibia Extensor MNs. Overall, Extension Position Sensing Neurons Could Activate Flexion and Inhibit Extension. Synaptic Weights Are Shown Between Connections Also Indicated by the Edge Thickness.

Proprioceptive Feedback to 13A Neurons

We identified sensory feedback from position-sensing proprioceptors to primary 13A neurons. Claw neurons detect position, while hook sense movement direction[73-75]. We examined reconstruction of proprioceptive neurons[15] and found multiple connections from flexion-sensing claw and hook neurons onto the main neurite of 13A-10f-α, which targets tibia flexor MNs (Figures 3D and Figure 3—figure supplement 3). Similar connections were observed onto 13A-10e-δ, -9d-γ. Recent connectome analysis showed that flexion sensing proprioceptors send direct excitatory feedback to tibia extensor MNs and indirect inhibitory feedback to flexor MNs[23]. Thus, flexion-sensing proprioceptors activate primary 13A neurons to inhibit tibia flexor MNs, while directly activating extensor MNs. Similarly, claw extension neurons connect to two 13A neurons that target tibia extensor MNs, while directly activating flexor MNs. Since these two groups of 13A neurons receive proprioceptive feedback and reciprocally inhibit each other, they could drive flexion-extension alternation.

Behavioral Evidence for Muscle Synergies During Grooming

Dusted flies use their legs to perform precise grooming actions, involving repeating patterns of body sweeps and leg rubs[1,2]. Quantifying these movements using machine vision methods (DeepLabCut)[76] reveals synchronized changes in angular velocity across multiple leg joints. During leg rubbing, proximal and medial joints move predominantly in sync, though they occasionally move asynchronously during head sweeps (Figure 4A). This coordination shows the presence of muscle synergies, and generalist premotor interneuron connectivity could be how these synergies are implemented.

13A Neurons Affect Limb Coordination During Grooming

Half of the 13A population expresses a transcriptional factor, Dbx[18]. We used Split GAL4 combinations to target smaller subsets, intersecting with a GAD line and Dbx to manipulate a small subset of 13A neurons.

These 13A neurons (Figure 4B and Figure 1—figure supplement 1B) target MNs controlling proximal extensors (Sternotrochanter extensor, tergotrochanter, tergoplural promotor body wall muscles, and trochanter extensor MNs), medial joint extensor/flexor MNs, and distal joint tarsus extensor MN (Figure 4—figure supplement 1A1-1A3). Based on their connectivity, we hypothesized that continuously activating them might reduce extension and increase flexion. Conversely, silencing them might increase extension and reduce flexion.

We measured changes in extension and flexion with joint positions, angles and inter-leg distances. Activating or silencing six 13A neurons reduced total grooming time and disrupted joint positions (Figure 4—figure supplement 1G'-1H') in dusted flies. Activation reduced proximal inter-leg distance, while silencing increased it (Figures 4D and 4E).

The frequency of extension-flexion cycles decreased with both manipulations, and the leg movements became slower and more variable (Figures 4H, 4I). In contrast, activating these 13A neurons during walking did not affect frequency of extension-flexion cycles but reduced walking speed in dusted flies (Figure 4—figure supplement 1K). Silencing specific 13A neurons in dusted flies disrupted both spatial and temporal features of grooming, highlighting their necessity in producing precise grooming actions.

Optogenetic manipulation of two different Dbx-positive 13A neurons also disrupted grooming, reducing joint position precision, median frequency, and maximum angular velocity during grooming (Figure 4—figure supplement 2 and Figure 1—figure supplement 1C).

Thus, 13A neurons regulate both spatial and temporal aspects of leg coordination during grooming.

13B Neurons Affect Limb Coordination During Grooming

Our experiments demonstrated that silencing or activating 13A and/or 13B neurons reduced grooming. Connectome data revealed that 13B neurons disinhibit motor pools. We generated a split GAL4 line that labels three 13B neurons (Figure 4C, Figure 4—figure supplement 3, and Figure 1—figure supplement 1D), which inhibit a primary 13A neuron (13A-9d-γ) that targets proximal extensor and medial joint flexor MNs (Figure 4—figure supplement 3C). One of these 13B neurons is premotor, inhibiting both proximal and tibia extensor MN. Together, these 13B neurons disinhibit proximal extensor and medial flexor MNs while inhibiting medial extensor MNs.

Activating or silencing these three 13B neurons in dusted flies also reduced grooming and resulted in joint positioning defects during grooming (Figure 4—figure supplement 3 D', E'). Silencing 13B neurons decreased proximal inter-leg distance (Figure 4G), similar to 13A activation (Figure 4D). Continuous activation of 13B neurons also reduced proximal inter-leg distance: we often observed that one leg became locked in flexion while the other leg remained extended, (indicating contribution from additional unmapped left right coordination circuits).

Manipulating 13B neuron activity also affects temporal aspects of grooming. Optogenetic silencing of 13B neurons strongly decreased median frequencies of all joints (Figure 4K), while activation slightly reduced median frequency and increased variability (Figure 4J). Both silencing or continuous activation decreased bout duration of head sweeps and leg rubs in dusted flies (Figure 4—figure supplement 3 F, G).

Together, 13A and 13B neurons contribute to both spatial and temporal coordination during grooming.

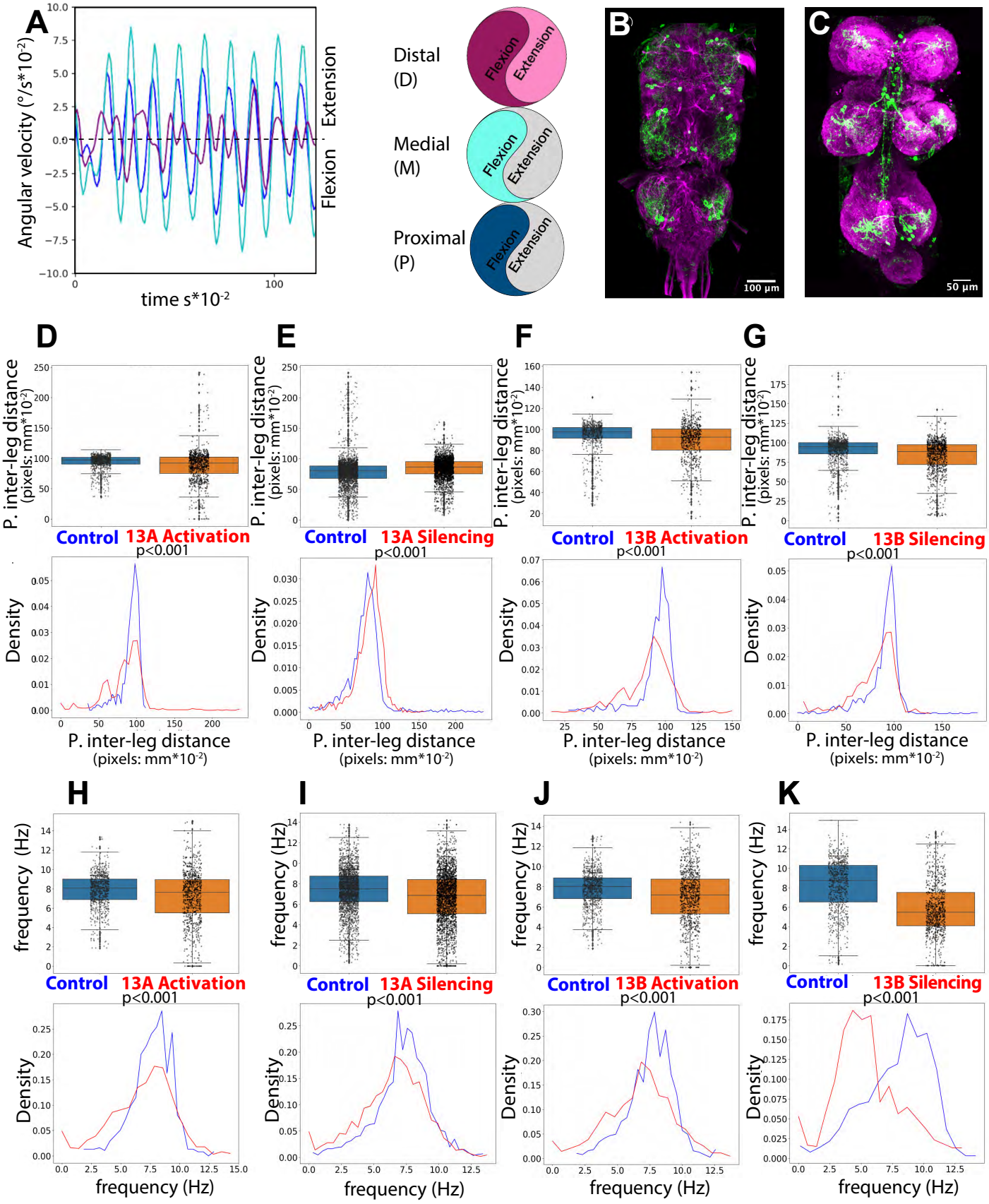

Figure 4. 13A and 13B Neurons Are Required for Leg Coordination During Grooming

(A) **Intra-joint coordination and muscle synergies:** Angular velocities of proximal (P, blue), and medial (M, cyan) joints predominantly move synchronously, while distal (D, purple) can move in or out of phase during leg rubbing.

(B) **Neuronal labeling of 13A neurons:** Confocal image showing six Dbx positive 13A neurons per hemisegment labeled by GFP using *R35G04-GAL4-DBD, Dbx-GAL4-AD* in VNC. Neuroglian (magenta) labels axon bundles.

(C) **Neuronal labeling of 13B neurons:** Confocal image showing three 13B neurons per hemisegment labeled by GFP using *R11B07-GAL4-DBD, GAD-GAL4-AD*. Nc82 (magenta) labels neuropil.

(D-K) **Effects of neuronal activity manipulation:** Activation and silencing of 13A neurons in dusted flies using *R35G04-GAL4-DBD, Dbx-GAL4-AD with UAS CsChrimson or UAS Kir*, respectively (n=19 activation, n=12 silencing). Control: *AD-GAL4-DBD Empty Split* with *UAS CsChrimson or UAS Kir*. For 13B neurons, *R11B07-GAL4-DBD, GAD-GAL4-AD* with *UAS CsChrimson or UAS GtACR1*, respectively (n=9 activation, n=7 silencing); control: *AD-GAL4-DBD Empty Split* with *UAS CsChrimson or UAS GtACR1*. Box plots show control data (blue) and experimental data (orange), each dot represents one segment, density of data distribution shown below box plots on y-axis and values along x-axis, control (blue), experimental (red), with significant effects ($p < 0.001$).

(D-G) **Proximal inter-leg distance:** Distance between femur-tibia joints of left and right front legs changes during head grooming. P inter-leg distance decreases with 13A activation (D), increases with 13A silencing (E), and decreases with both 13B activation (F) and silencing (G).

(H-K) **Frequency modulation:** Silencing or activating 13A or 13B neurons reduces median frequency of proximal joints in dusted flies. Increased variability indicated by a broader interquartile interval. 13B silencing reduces median frequency from ~8 Hz to ~5 Hz.

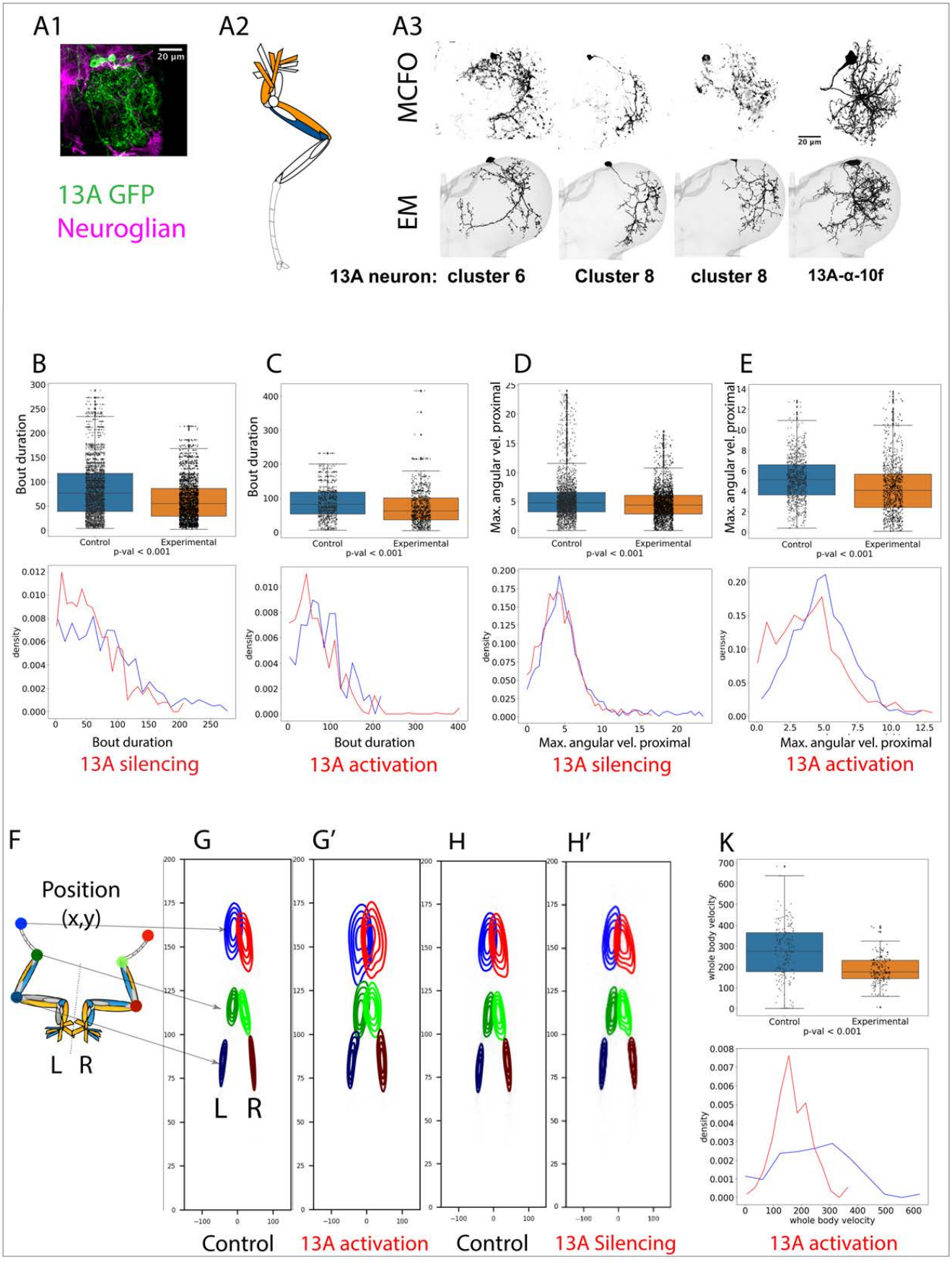

Figure 4—figure supplement 1. 13A Neurons Regulate Leg Coordination During Grooming and Walking

Neuronal labeling and connectivity: (A1) A confocal image showing six Dbx positive 13A neurons/hemisegment labeled by GFP driven by *R35G04-DBD, Dbx-AD Split GAL4.* T1 right front leg neuropil of the VNC is shown. GFP (green) labels 13A neurons. Neuroglian labels axon bundles in magenta. (A2) Schematic illustrating all muscles controlled by the motor neurons inhibited by specific 13A neurons. (A3) Top panel shows confocal images showing multicolor flip out clones (MCFO) (Nern et al., 2015) of 13A neurons. Bottom panel shows corresponding EM reconstructions of 13A neurons that resemble MCFO clones.

Manipulating activity of Six Dbx positive 13A Neurons: Silencing and activation of 13A neurons in dust-covered flies using *R35G04-DBD, Dbx-AD Split Gal4 > UAS Kir and UAS CsChrimson*, respectively. Control conditions include *AD-DBD Empty Split* for inactivation and *AD-DBD Empty Split with UAS CsChrimson* for activation. 13A inactivation (n=12 experimental flies/47 videos), activation (n=19 experimental flies/46 videos). Box plots showing control data in blue and experimental in orange, with the density of the data distribution shown below the box plots on the y-axis and values along the x-axis, control in blue, experimental in red. Significant effects observed in all analyzed cases ($p < 0.0001$).

(B, C) Reduction in head grooming bout duration ($s*10^{-2}$) during silencing (B) and activation of 13A neurons (C).

(D,E) Maximum angular velocity ($° /s*10^{-2}$) of the proximal joint reduces during silencing (D) and and upon continuous activation (E) of 13A neurons.

(F-H') Joint Positions: Schematic showing position of various joints of the front legs is shown in F. Contour plots (probability distribution of joint positions) of the front legs of all the control and experimental flies during head grooming. The position of leg terminal (tarsus tip) is shown in colors: left leg in blue, right in red, the distal joint in dark and light green, and medial joint in dark blue and maroon. Joints positions are significantly altered ($p<0.001$) upon activation of 13A neurons (G'), and slightly upon silencing (H') of 13A neurons in dust-covered flies.

(K) Whole body velocity (pixels[or $mm*10^{-2}$]/s) decreases upon 13A activation during walking in dust covered flies.

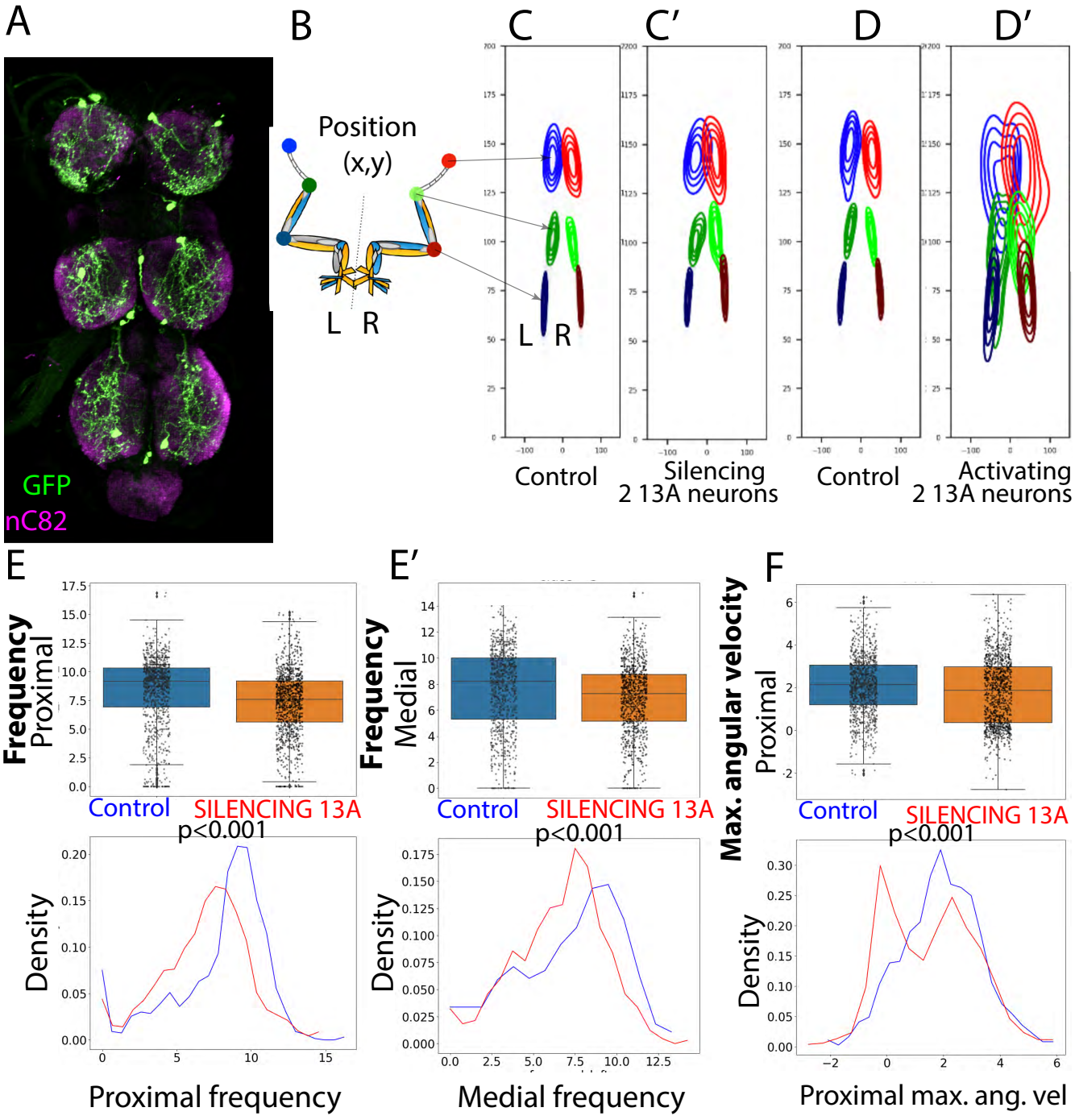

Figure 4—figure supplement 2. Two Dbx Positive 13A Neurons Are Involved in Leg Coordination During Grooming in Dust-Covered Flies

(A) Confocal image showing two Dbx positive 13A neurons/hemisegment labeled by GFP driven by *R11C07-DBD, Dbx-AD Split GAL4* in the adult VNC, labeled by GFP (green). nC82 (magenta) labels synaptic neuropil.

(B-G) Effects of manipulating activity of two 13A neurons: Silencing and activation experiments in dusted flies using *R11C07-DBD, Dbx-AD Split Gal4 > UAS GTACR1 and UAS CsChrimson*, respectively. Control conditions include *AD-DBD Empty Split* with *UAS GTACR1* for inactivation and with *UAS CsChrimson* for activation. 13A inactivation (n=7 experimental flies/40 videos), activation (n=4 experimental flies/18 videos). Significant effects observed in all analyzed cases ($p < 0.0001$).

(B-D') Contour plots (probability distribution of joint positions) of the front legs during grooming actions. Joints positions are significantly altered upon silencing (C') and activation of 13A neurons (D') in dust covered flies. Joint positions are shown during head sweeps (C-D').

(E,E') Median frequency (Hz) of the proximal and medial joints decreases upon silencing of two 13A neurons

(F) Maximum angular velocity (° /s*10^{-2}) of the proximal joint reduces upon silencing of two 13A neurons.

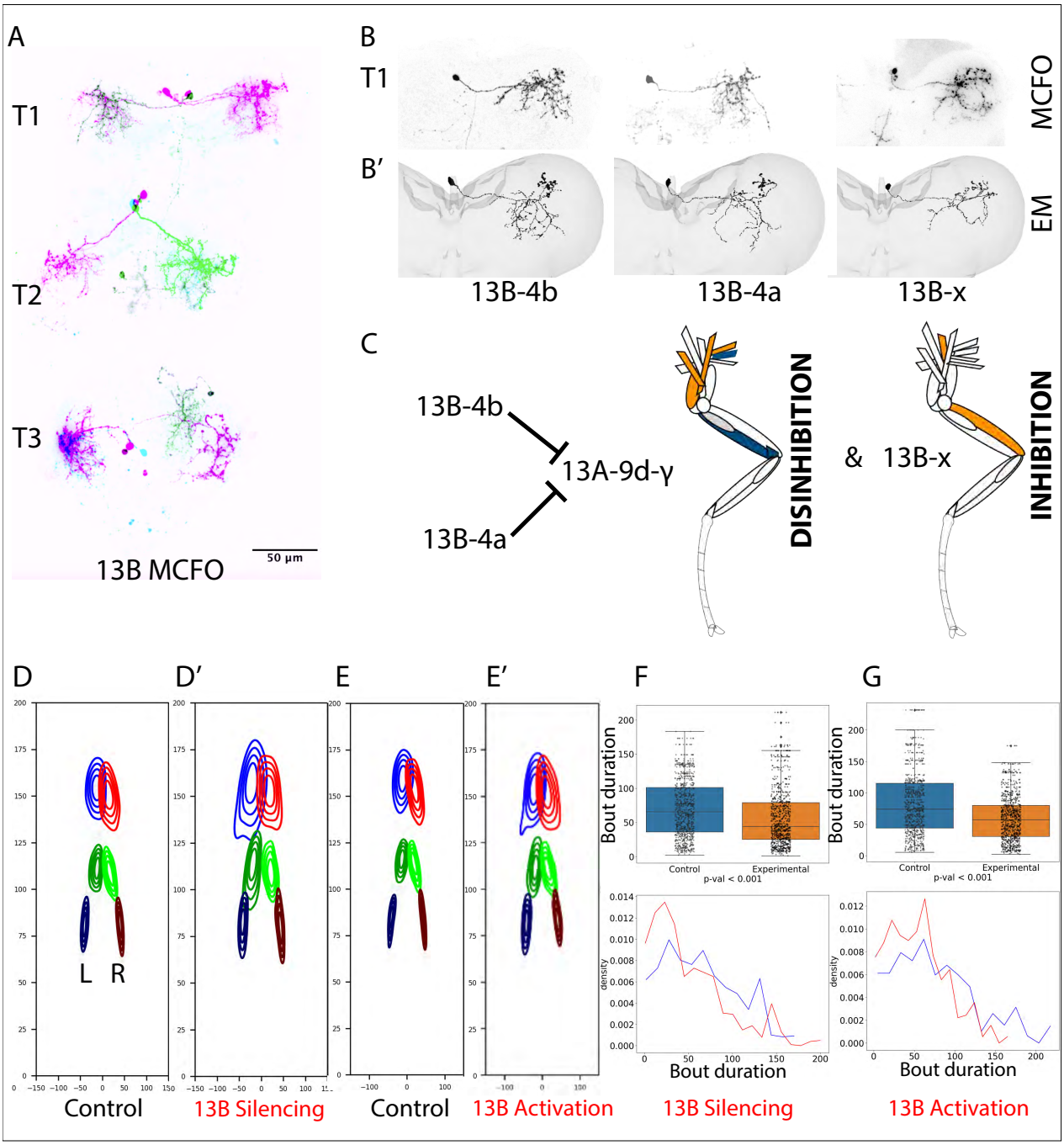

Figure 4—figure supplement 3. Neuronal Labeling. Connectivity and Behavior of Specific 13B Neurons

(A) Neuronal labeling: A confocal image showing clonal analysis of 2-3 13B neurons labeled in each hemisegment of the adult ventral nerve cord by *R11B07-DBD, GAD-AD Split GAL4.* Multicolor flip-out (MCFO) clones of all the 13B neurons labeled are shown in purple, green and black.

(B) MCFO clones of individual 13B neurons labeled in the right T1.

(B') EM reconstructions of 13B neurons in right T1 that resemble these MCFO clones.

(C) Muscle targets disinhibited by two of these 13B neurons and those inhibited by one 13B neuron. Proximal extensor MNs and medial flexor MNs are disinhibited while medial extensors are inhibited. Extensor muscles in orange and flexor in blue.

(D-E') Contour plots (probability distribution of joint positions) of the front legs during grooming actions. Joints positions are significantly altered upon silencing (D') and activation of 13B neurons (E') in dust covered flies. Joint positions are shown during head sweeps (D-E'').

(F-G) Reduction in head grooming bout duration ($s*10^{-2}$) upon silencing (F) and activation of 13B neurons (G).

Activation of Inhibitory Neurons Induces Rhythmic Leg Movements

Connectome analysis revealed that inhibitory 13A and 13B neurons frequently synapse onto 13A premotor neurons. Thus, activation of these 13A or presynaptic 13B neurons should inhibit postsynaptic 13A neurons, releasing activity in MNs and promoting movement. Indeed, we observe that optogenetic activation of specific 13A and 13B neurons triggers grooming movements.

We also discover that the timing of 13A activation influences frequency of these rhythmic grooming actions. Anterior grooming actions in dusted flies are rhythmic where leg rubbing and body sweeps typically occur at a median frequency of ~7-8 Hz. One complete extension and flexion cycle, representing one sweep or leg rub, lasts ~140 ms, with 70ms extension and 70ms flexion phases (Figures 5B and 5B'). Connectivity analysis suggests that specific 13A neurons would be tuned to induce extension and others induce flexion, with reciprocal inhibition potentially generating rhythmicity. We optogenetically activated specific 13A neurons using 70 ms on and off light pulses, to mimic the flexion-extension cycle, in clean flies. This indeed induced grooming (anterior and posterior) and walking (Figures 5C-5F, Figure 5—Video 1). This experimental evidence shows that 13A neurons can generate rhythmic movements, reinforcing their role in coordinating grooming behavior.

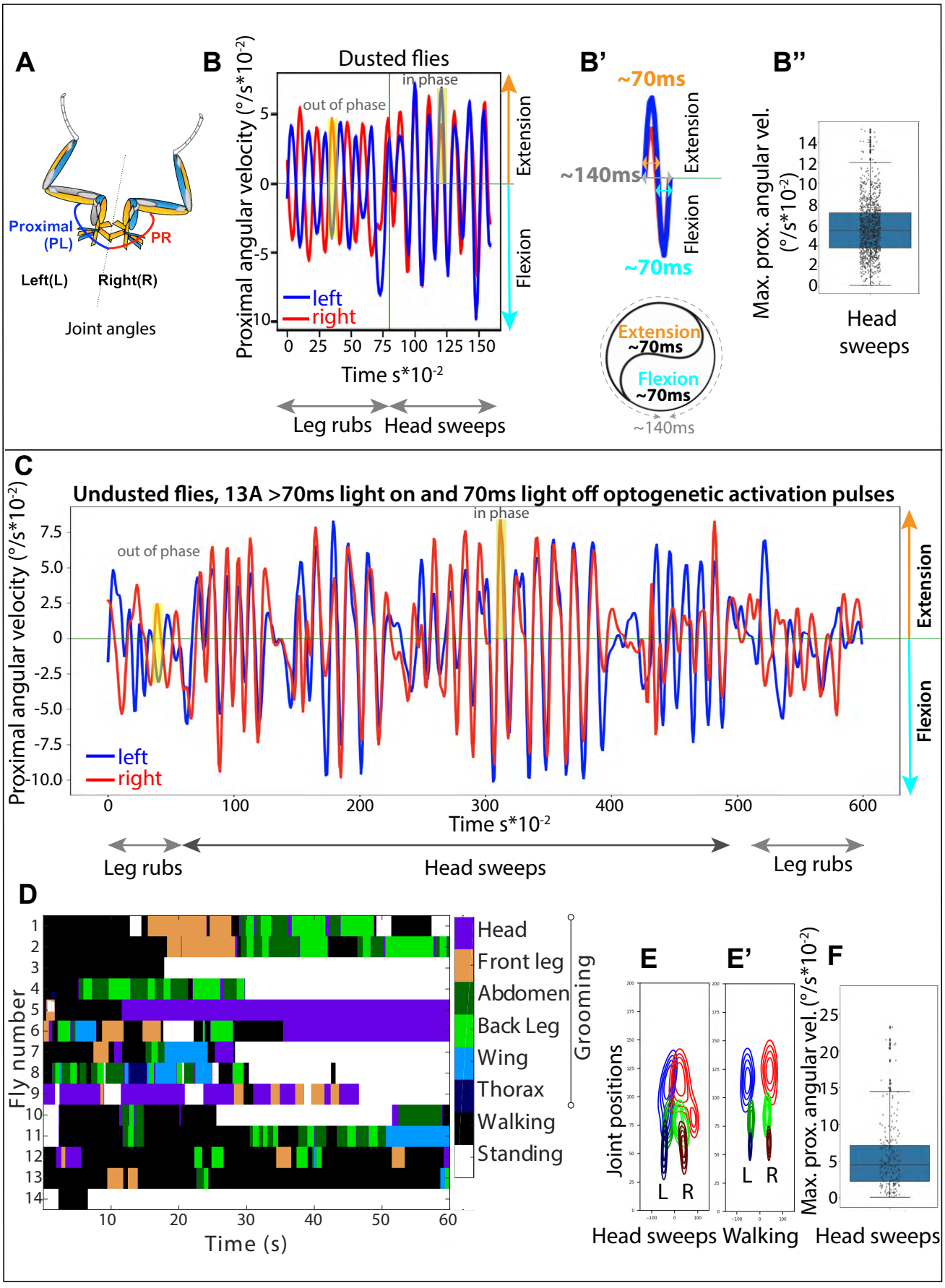

Figure 5. Pulsed Activation of 13A Neurons Triggers Rhythmic Actions in Clean Undusted Flies

(A) Schematic showing proximal joint angles of left (PL) and right (PR) legs

(B) **Left-right coordination and muscle synergies during anterior grooming.** Dusted flies perform alternating leg rubs and head sweeps. Proximal joint angular velocities are shown. PL (blue) and PR (red) joints move anti-phase during leg rubs and in-phase during head sweeps (highlighted yellow box). Positive values indicate extension, and negative indicates flexion. (B') Each flexion and extension cycle lasts ~140 ms, with each phase around 70 ms. (B'') Maximum angular velocity of proximal joint during head sweeps.

(C-F) Effect of optogenetic activation using 70ms on and 70ms off pulses in specific 13A neurons (*R35G04- DBD, Dbx-GAL4-AD >UAS CsChrimson*) in undusted flies.

(C) Angular velocity of PL and PR leg joints shows anti-phase leg rubs and sustained in-phase head sweeps, with light pulses active from time=0.

(D) Behavioral ethogram showing various grooming actions and walking triggered by 70ms on and 70ms off pulsed activation of 13A neurons in undusted flies, with light pulses on from time=0.

(E) Joint Positions: Contour plots (probability distribution of joint positions) of front legs in undusted flies during head grooming (E) and walking (E') upon pulsed 13A activation, with tarsus tip positions in blue for left leg (L) and red for right leg (R), distal joints in dark and light green, and the medial joint in dark blue and maroon.

(F) Maximum angular velocity of proximal joint during head sweeps upon pulsed 13A activation in undusted flies, comparable to that observed in dusted flies (B'').

Figure 5—Video 1 Activation of six 13A neurons with 70ms on and 70ms off pulses in undusted flies induces grooming and walking behaviors. In this video, light pulses start at t=30s with a pattern of 70ms on and 70ms off. Light is off from t=0-30s.

A Computational Model of Inhibitory Circuits in Coordinating Grooming Actions

The inhibitory circuits connecting to MNs are complex and genetic reagents to target their individual components are limited, so figuring out how each component contributes to leg coordination experimentally is challenging. We developed a neural computational model based on anatomical connectivity to explore potential circuit functions. We modeled groups of functionally related neurons. For example, 13As that are inhibiting each other represent two groups modeled as two nodes – Figure 6A shows such a circuit for a single joint. This approach is loosely inspired by Jovanic et al., 2016[77]. Since we are not modeling individual neurons, the network does not involve spiking neurons but rather "rate based" units. The "synaptic weights" of the model network correspond to number of synapses obtained empirically from connectome (Figure 6A).

The neural network controls movements of virtual front legs of an agent, where each leg is simplified to a 2D configuration of three segments. A pair of antagonistic "muscles" controls each of the three "joint" angles on each leg. These pairs of muscles determine the angular velocities of each "joint." Thus each leg receives inputs from six virtual MNs. These MNs receive descending excitatory inputs, and inhibitory inputs from two 13A nodes (inhibiting the MNs of flexors and extensors). The states of the muscles (amounts of extension or flexion) are sensed by sensory neurons (SNs) that provide feedback to the 13As and to MNs. As the legs move, the most distal "joint" removes the virtual dust (Figure 6I). Legs must also spend some time in proximity to each other to remove the "dust" from themselves (This constraint forces the legs to coordinate with each other.).

The excitatory input to the model circuit is a function of the distribution of "dust" remaining on the "body" - the environment (the green areas in Figure 6I). The response to this environment is produced by a linear recurrent neural network (RNN) that transforms the distribution of the "dust" into excitatory inputs for the 13A network. This simple RNN is a "black box" used to provide the 13A circuits with excitatory sensory inputs so that the agent can respond to the changing environment. But the 13A circuitry can still produce rhythmic behavior even without those external sensory inputs (or when set to a constant value), although the legs become less coordinated.
The model neurons either reach the ceiling values or zero. We also added 13B nodes, as shown in Figure 6A. These nodes receive inputs from the same 'black box' as 13As.

To study the contribution of the 13A circuits to the grooming behavior we could have applied a periodic excitatory "descending" input and observe how the 13A circuits transform that input into behavior. However, to explore the possibility of de novo emergent periodic behavior (without the direct periodic descending input) we instead varied the model's parameters around their empirically obtained values. We could do this because our empirically derived weights are not exactly represented by the weights of the modeled network. So, we "fine-tune" the weights, subject to constraints based on empirical values: the signs of the fine-tuned weights must remain the same as the empirical synapses (e.g. inhibitory neurons remain inhibitory), and their magnitudes must be at least 80% of the empirical weights. Fine-tuning procedure is accomplished by genetic algorithms library PyGAD (https://pygad.readthedocs.io/en/ latest/

index.html). The fitness function is defined as the total amount of virtual dust that the model agent removes across several episodes of grooming. The fine-tuned weight matrices and the original ones are shown in Figures 6B-6C. Note how the ratios between synaptic weights are largely preserved.

After the fine-tuning, we analyzed the activity of the modeled 13A neural circuits, and the behavior it produced. Figure 6I shows the first, middle, and last frame of a movie. The agent succeeded in removing most of the dust (the green pixels). Figures 6D-6F shows the angles and angular velocities of the three "joints" of each front leg, and Figures 6G, 6H show the corresponding neural activity of the 13A neurons. Notice the periodic patterns in both, the motor output and the firing rates of the 13A nodes.

Next, we inquired how the model responds to perturbations analogous to the experimental activations of the 13A neurons. Figure 6J shows the dynamics of left leg joint angles in 100 renditions, when no stimulus is applied. Notice the regular periodicity of these dynamics. As we vary the length of activation pulses (Figure 6K), behavior, as reflected in angle dynamics, becomes distorted. (Legs also lose coordination and consequently less dust is removed.) These distortions also involve higher frequency of movements (see angular velocities in Figure 6K).

We also tried removing individual synaptic connections: removal of either one of the reciprocally inhibiting connections between 13As of a leg completely paralyzes it. Removing all 'proprioceptive' feedback from SNs to MNs does not stop the execution of the periodic movement, but it slows it down (Figure 6—figure supplement 1). Obliterating all 13A → MN synapses, not surprisingly, completely paralyzes the leg. Interestingly, removing 13As-ii—MN connections to the three MNs (second row of the 13A → MN matrices in Figures 6B,C) does not have much effect on the leg movement (data not shown). It seems sufficient for this model to contract only one of the two antagonistic muscles per joint, while keeping the other at a steady state. Thus, our computational model confirms that rhythmic movements could be produced by inhibitory 13A circuits (even without external sensory inputs from the dust, or patterned descending input). By replicating leg movements based on real anatomical connectivity, we investigated the functional roles of specific circuit components. This platform enhances our understanding of role of inhibitory circuits in leg coordination during grooming, providing a foundation for generating informed hypotheses in future experimental studies.

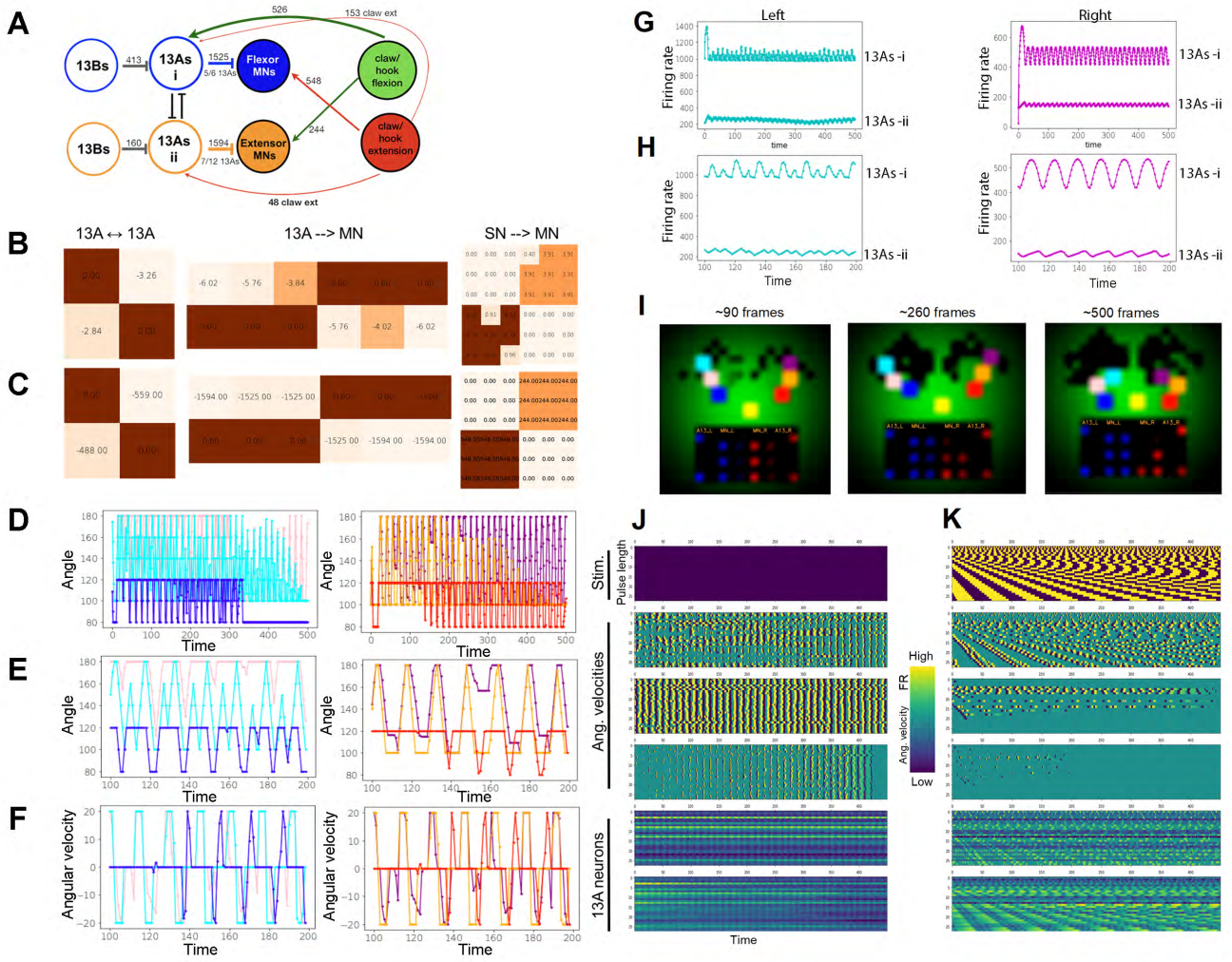

Figure 6. Modeling the 13A Circuits.

(A) Circuit diagram showing inhibitory circuits and synaptic weights based on connectome.

(B) Adjacency matrices of the model circuits (after fine-tuning).

(C) Adjacency matrices from the empirically estimated weights, indicated in the simplified circuit diagram in (A).

(D) The three "joint" angles of the left leg (left) and the right leg (right) as they change over the time of one episode (500 frames). Colors indicate "joint" angles in the same order as in (I).

(E) Same as (D) but zoomed-in to between 100-200 frames.

(F) Same as (E) but showing angular velocities.

(G) Firing rates (activity levels) of the two 13A neurons over one episode (500 frames), for both legs (left, right).

(H) Same as (G) but zoomed-in to between 100-200 frames.

(I) Video frames from the beginning, middle, and end of a video of one episode. Left leg is represented by three “joints”: distal (cyan), medial (pink), and proximal (blue). Right leg: distal (purple), medial (orange), and proximal (red). The legs originate from the “base” (yellow). As legs move over the “body” (the environment – dust is represented as the green Gaussian distribution), the dust (green) is getting removed (black background). The bottom of each movie frame shows the activity of the two left 13A nodes and six left MNs (blue). The right leg nodes are shown in red, on the right side. Brightness of the nodes indicates the activity level. See Video1.

(J) The dynamics of angular velocities of the left leg’s “joints”, and left 13A activation levels, over 100 episodes (500 frames each), when no stimulus is given (indicated by empty matrix on the top). Each row of each matrix is one episode.

(K) Same as in J, but stimulation with pulses of varying durations is given. Top row of each matrix: pulse duration=2 frames; bottom (100th) row of each matrix: pulse duration=100 frames. The pulse stimulation is indicated in the top matrix.

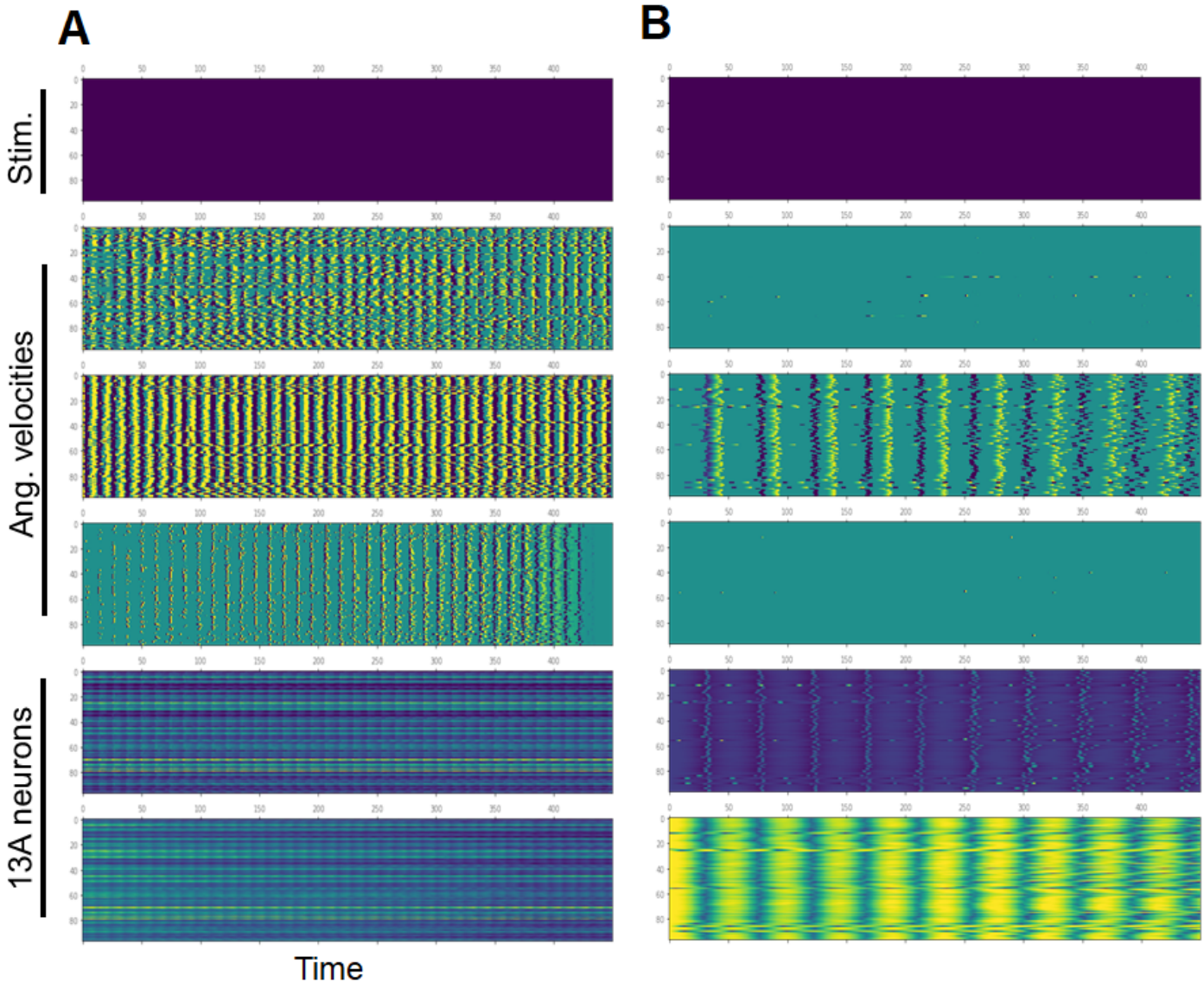

Figure 6—Figure Supplement 1. Modeling the 13A Circuits.

(A) Dynamics of angular velocities and 13A neurons, when no stimulus is given (Similar to Figure 7 J).
(B) Same as A, but with proprioceptive SN → MN feedback connections obliterated.

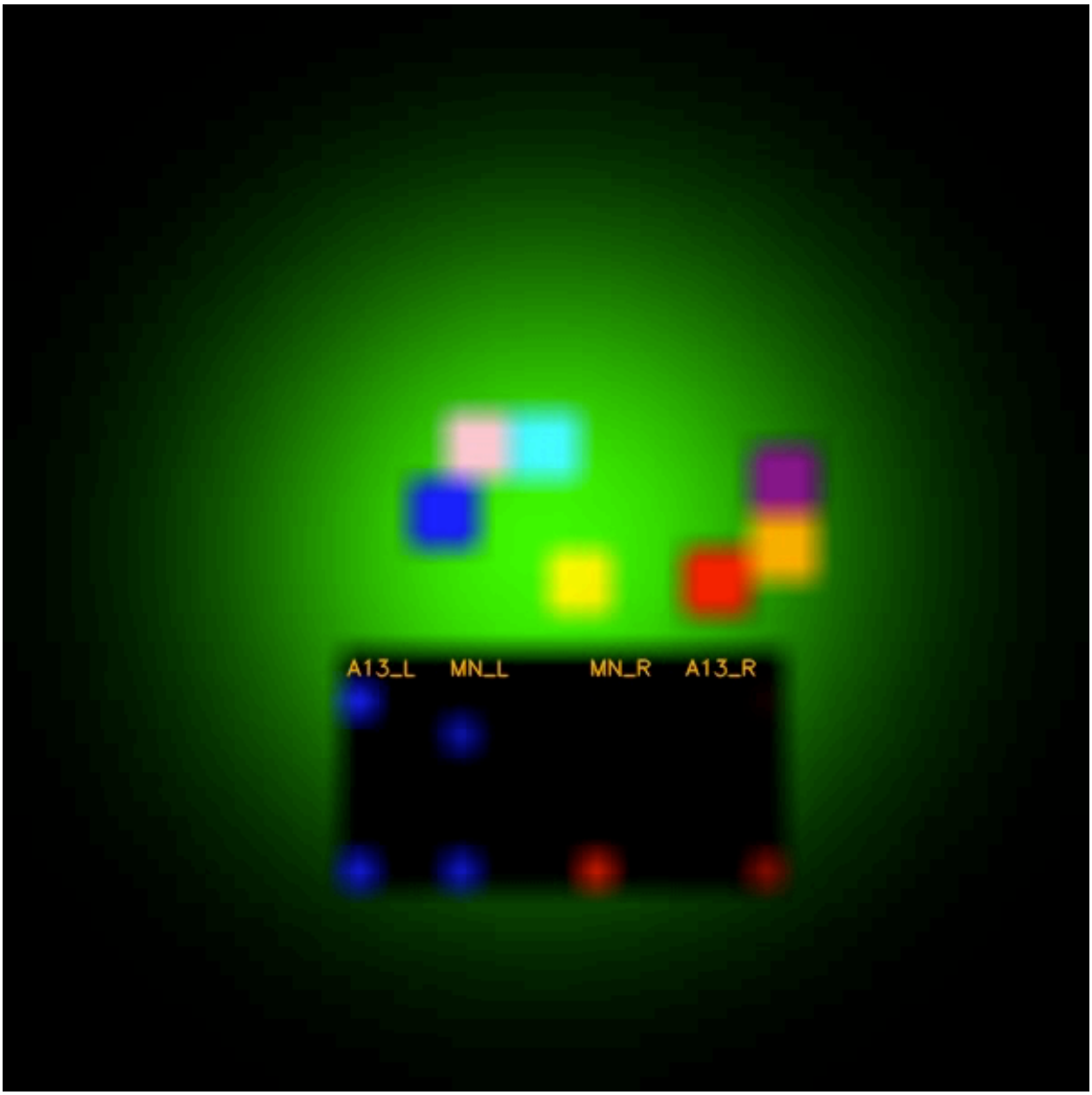

Video 1. **Modeling the 13A circuits.** Description in Figure 6I.

Table S1: 13A and 13B Neurons in the Front Leg Neuromere

DISCUSSION

Inhibitory Circuit Motifs

Using VNC EM connectome data, we identified various circuit motifs formed by 13A/B inhibitory neurons that contribute to motor control.

Feed-forward inhibition: Generalist 13A neurons synapse onto multiple MNs influencing broad movements like whole leg extension, while specialist 13A neurons refine joint-specific movements.

Disinhibition: 13A neurons targeting extensor MNs connect to 13As targeting flexor MNs, enabling flexor activation when extensors are inhibited. Generalist mediated disinhibition coordinates muscle synergies across joints, promoting leg extension or flexion. Some 13B neurons provide direct inhibition (Figure 3A), while others have an indirect effect by disinhibition of motor pools. This disinhibition motif, similar to those observed in motor systems for sequence selection[77-84] and flight regulation[85], may prime motor responses by holding them at the ready, to be released when inhibition is removed.

Reciprocal inhibition: 13A neurons inhibiting flexors and extensors within a leg are reciprocally connected (Figure 3). This circuit resembles rIa-inhibitory neurons and reflects reciprocally connected circuits involved in vertebrate locomotor rhythm generation[85-92].

Redundant inhibition: Inhibitory neurons target both MNs and their excitatory pre-synaptic partners, creating coordinated control. For example, 13A-10f-α connects to both tibial flexor MNs and excitatory premotor neurons (20A/3A) that activate flexor MNs (Figure 2—figure supplement 4), preventing their activation. Similarly, the 13B-4i neuron connects to 13A neurons inhibiting flexor MNs, leading to disinhibition (Figure 3—figure supplement 2), and to excitatory neurons presynaptic to 13A neurons.

Proprioceptive feedback onto inhibitory circuits

Position-sensing proprioceptors connect to 13As, which inhibit flexion and disinhibit extension and vice versa, complementing reciprocal inhibition to generate alternation. Movement-sensing proprioceptors synapse onto 13A neurons, but are suppressed during walking and grooming[93]. Sherrington's 1910 proposal, supported by spinal cat studies, suggests proprioception triggers alternation—a mechanism observed in rhythmic behaviors like locust flight and mammalian respiration[95-100]. Connections between position sensors, 13A neurons, and antagonistic MNs suggest that proprioceptive signals may trigger alternation of leg movements during grooming.

Local and descending neurons presynaptic to reciprocally connected 13A neurons could also induce alternation. The balance between internal circuits within the central nervous

system and sensory feedback contributes to pattern generation. Future studies will dissect the extent of peripheral verses central control in generating alternation.

These motifs explain the spatial and temporal dynamics of grooming movements. **Flexors and extensors at multiple joints must coordinate to fully extend or contract a leg.** Neurons targeting related MNs could facilitate synchronization. For example, cluster 6 or 8 13A neurons target proximal and medial joint extensor MNs, allowing leg flexion. During head sweeps, proximal and medial joints move independently—for example, the proximal joint flexes while the medial joint extends—which can be coordinated by cluster 10 13A neurons and 13A-9e, -9f.

Flexors and extensors should be mutually exclusive. A generalist connected to both proximal and medial joint MNs could facilitate leg rubbing. For example, 13A-10c synchronously inhibits proximal, medial and distal flexor MNs (Figures 3C and Figure 2—figure supplement 1I4) while targeting 13A neurons (13A-8a, -8b, and 8c) connected to extensor MNs (Figures 3F and Figure 2—figure supplement 1 G1-G3). This arrangement ensures inhibition of MNs and disinhibition of antagonistic MNs across multiple joints, preventing simultaneous coactivation.

Flexors and extensors should alternate. Reciprocal inhibition and proprioceptive feedback onto 13A neurons could facilitate alternation. Reciprocal inhibition between generalist neurons of 13As-i and 13As-ii could induce alternation during head sweeps (Figure 3D). This aligns with half center model that proposes the activity of flexors and extensors is produced by two interconnected half-centers[101-103]. Our behavior experiments and modeling further support this connectivity, as we indeed induced rhythmic motion through pulsed activation of specific inhibitory neurons without altering any excitatory drive.

Inhibitory Innervation Imbalance Between Flexors and Extensors

We observed an imbalance in the innervation: more 13A neurons target extensors across multiple joints. While legs alternate between extension and flexion, they remain elevated during grooming. To maintain this posture, some MNs must be continuously activated while their antagonists are inactivated. Uneven distribution of inhibition could ensure that while some MNs remain active, others alternate flexion and extension in a controlled manner. Among the 13A neurons inhibiting antagonistic muscles, reciprocally connected ones could induce alternation, while others could keep legs elevated.

The asymmetry in connections, with more 13B neurons disinhibiting flexor-inhibiting 13As, suggests a mechanism for preferential control of flexion, supporting the flexor burst generator model, where the generator actively excites flexor MNs while inhibiting tonically active extensors[104,105].

Spatial Mapping of premotor neurons in the nerve cord

Our study highlights spatial organization of 13A neurons connecting to MNs across multiple joints. 13A neurons with similar morphologies target the same MN sets, indicating organized mapping of outputs and inputs. This topographic map aligns with the wiring economy principle, suggesting that circuits are structured to minimize neurite length and energy costs while maximizing efficiency[106-109]. Such organization likely arises from evolutionary pressures to enhance overall fitness resembling spinal modules, which coordinate distinct motor outputs[33,110]. For evolutionarily conserved repetitive movements like grooming, this arrangement could minimize conduction delays and optimize energy usage.

Computational modeling of inhibitory circuits

We employ a linear rate-based (non-spiking) neural network to represent the 13A circuitry. Natural behavior and neural activity are of course more complex. Our model explores how 13A circuit motifs could contribute to, or produce de novo, behavioral features, including rhythmic movements (which might be normally produced by upstream circuits), in 2D space, matching the dimensionality of our behavioral data. This abstraction is inspired by Jovanic et al, 2016[77], but we add the agent component to the neural circuitry, and apply evolutionary "fine-tuning" of parameters. When we perturb the model by activating 13A neurons with varying pulse lengths, we observe decreased coordination and increased movement frequency (compare angular velocities in Figure 6J with Figure 6K). Here we did not attempt to simulate the exact experimental procedures. In future, model's parameters could be fine-tuned within similarly constrained space, but with the fitness function modified: instead of parameters being optimized to remove "dust", they could be optimized by the similarity of behavioral features between the model and real flies, as has been done in whole-animal modeling[110], under various experimental conditions.

Future Directions

Our work lays groundwork for future exploration of inhibitory circuits in motor control. Developing genetic tools to target specific inhibitory motifs and functional imaging during behavior would allow us to correlate temporal neuron activation with limb motion. While we focus on inhibitory control of one leg, manipulating these neurons reveals defects in left-right coordination. Investigating the circuitry involved in this coordination —possibly mediated by commissural and/or descending neurons connected to these circuits—will be interesting. Pulsed activation of 13A neurons induces grooming or walking in clean flies, while manipulating their activity in dusted flies alters grooming timing. This suggests that 13A neurons may be part of central pattern generators. Other neural circuits, not yet identified, may also contribute to the generation of rhythmic leg movements. Future studies should identify neurons that regulate rhythmic timing and their interactions with inhibitory circuits.

Our connectome analysis and clustering of new EM data reveal that inhibitory neurons within a hemilineage form diverse circuit motifs with complex connections to specific leg motor neurons. These neurons likely complement excitatory premotor circuits, enabling multifunctionality in behaviors such as grooming and walking. Their connectivity suggests roles in coordinating movements across multiple joints, enforcing flexor/ extensor muscle antagonism, and driving extension and flexion alternation. We model and extrapolate the potential functions of these complex inhibitory motifs. Normal activity of these inhibitory neurons is critical for grooming; silencing or continuously activating them reduces time spent and effectiveness in dust removal, leading to forced flexion or abnormal extension, with limbs locked in extreme poses. Moreover, we show that inhibition, independent of excitatory input, plays an instructive role in generating rhythmic leg movements. Although we focus on grooming behavior, we expect these motifs to also contribute to walking, as the leg must recruit the same limited motor and premotor components to generate diverse movements. We conclude that inhibitory neurons are essential for controlling flexible limb movements and may play a key instructive role in timing and coordinating rhythmic behaviors.

MATERIALS AND METHODS

Contact for reagent and resource sharing

For information and inquiries regarding resources and reagents, please write to the lead contact Julie H. Simpson (**jhsimpson@ucsb.edu**).

Experimental model and subject details

Drosophila melanogaster were raised on a standard cornmeal medium at 25°C in a 12 hr light/dark cycle. For optogenetic experiments, one day old flies were transferred to food containing 0.4 mM all-trans-retinal and kept in the dark for 3 days. Genotypes of the fly lines are included in the Key Resources Table.

Identification of fly lines that target inhibitory neurons

We visually screened the VNC expression of various GAL4 lines on Flylight database[111] and compared them to the inhibitory hemilineages[19]. Next we obtained corresponding *AD, and DBD* flies from BDSC for the candidate lines and crossed them with *GAD-GAL4-AD or GAD-DBD* (Haluck Lacin) to confirm and restrict their expression in GABAergic neurons. *R35G04-GAL4-DBD, GAD-GAL4-AD* labeled six 13A and six 13B neurons per hemisegment. We also isolated six 13A neurons from this line by using *R35G04-GAL4-DBD, DBX-GAL4-AD* combination. *R11C07-GAL4-DBD and GAD-GAL4-AD* labels 4 inhibitory neurons. We intersected *R11C07 DBD* with *Dbx AD* to isolate two 13A neurons. *R11B07-GAL4-DBD, GAD-GAL4-AD* labeled 3 13B neurons.

Immunofluorescence and confocal microscopy

Flies were immobilized by anesthetizing them on ice (4°C). Central nervous system (CNS) was carefully dissected in 1X Phosphate-buffered saline (PBS). Subsequently, the wings were removed, and the flies were positioned ventral side up on a Sylgard plate. All legs were excised, and fine forceps (No. 5 Dumont from FST, Switzerland) were employed to delicately open the thorax along the midline, taking care to avoid damaging the underlying thoracic ganglia. A small incision near the first abdominal segment ensured preservation of the abdominal ganglion. Surrounding tissues were cleared from the thoracic ganglia, which were then gently extracted by grasping the neck connective. The dissected thoracic ganglia were subsequently fixed in 4% buffered paraformaldehyde for 45 minutes at 4°C.

Post-fixation, the thoracic ganglia underwent three 15-minute washes in 0.1% Triton X-100 (PBT) at room temperature on a shaker at 60 rpm, followed by a 20-minute wash in 0.1% PBT with normal goat serum (blocking solution). Primary antibodies, diluted in 0.1% PBT-NGS, were applied to the samples and incubated overnight at 4°C on a horizontal shaker. Following primary antibody incubation, the samples underwent three 15-minute washes in 0.1% PBT and one 20-minute wash in 0.1% PBT-NGS . Secondary antibodies, diluted in 0.1% PBT-NGS, were added to the samples and incubated for 2-4 hours at room temperature on a shaker at 60 rpm. Secondary antibody removal was achieved through four 15-minute washes with 0.1% PBT at room temperature. Finally, the tissues were mounted on glass slides using Vectashield mounting medium (Vector Labs).

Primary antibodies used were Chicken pAb anti-GFP (Abcam, 1:1000), Rabbit (Rb) anti-GFP (Abcam, 1:1000), mouse (ms) anti-Neuroglian (BP104) (DSHB, 1:40), ms monoclonal anti-Brp antibody (nC82) (DSHB,1:200). For MCFO labeling experiments, Rb mAb anti-HA (Cell Signaling Technologies, 1:300), Rat anti-FLAG (Novus Biologicals, 1:200), DyLight549-conjugated anti-V5 (AbD Serotec; 1:300 dilution).

Secondary antibodies from Invitrogen Molecular Probes conjugated with Alexa-488, Alexa-568 and Alexa-647 raised against chicken, ms and Rb were used in 1:400 dilution.

Zeiss LSM710 confocal microscope was used to obtain images of the CNS. Images were then processed in FIJI.

Recording and analysis of grooming in clean and dusted flies

For open field assay, we dusted the flies and obtained the recording as previously described[4]. Constant light intensity of 5.6 mW/cm² was used for continuous activation. Automated behavior analysis (ABRS) was used to quantify the amount of time flies perform individual grooming actions[112]. Additionally, manual scoring was performed[2] in flies showing uncoordinated leg movements. Quantification and statistical analysis describing the percentage of time dusted flies spent doing grooming and uncoordinated leg movements upon 13A and B activity manipulation was performed in Matlab as previously described[4].

For limb tracking, either clean or dusted freely moving male flies were put in a studio containing 10-mm diameter quartz chamber and 100 Hz videos were recorded from below using FLIR Blackfly S camera. Custom-built LED panels (LXM2-PD01-0050, 625 nm) were utilized to deliver light activation from below, with an intensity of 1.1 mW/cm². Green led was used for silencing experiments.

Behavior analysis

Raw data, consisting of coordinates of the six annotated points on the front legs and two reference points on the body (per one frame of a video), was obtained from DeepLabCut[76]. From these coordinates we computed: 1) (fly-centric) spatial positions of the body parts, 2) the spatial velocities of the points, 3) the whole-body velocity (the translation, obtained from the reference points in absolute coordinates), 4) the euclidean distances between the leg points ("joints") and other "joints" or the reference points, and 5) the joint angles.

All behavior analysis was performed using Python, version 3.9.7.

Continuous feature extraction

The euclidean distances between various body parts (the six "joints" and the two reference points) are used as continuous features. The body velocity was computed as a euclidean distance of a point covered across a 50 frame (0.5 second) time window. Three joint angles per leg were computed from the three points on the leg and the two reference points. These angles are: posterior, medial, and distal angles. Angular velocities were computed as derivatives of the raw angles, and were lightly smoothed by a Gaussian filter (filter sigma = 2 frames). The euclidean distances were also smoothed by the same method.

The angular velocity time-series (AV) is used as the basic signal from which other continuous behavioral features are extracted, and also serves as the basis for segmentation. The main continuous features extracted from the AV are the phase and the frequencies.

The phase (between the movement of the front-legs) was computed from cross-correlation of AV signals of the two legs, using the signal.correlation_lags()function with the window for cross-correlation of five frames. We took the time-position of the maximum cross-correlation (the peak) as the lag (the phase). If the two legs are perfectly in-phase, the peak of the cross-correlation will be at time 0. The phase is a good indicator of a general type of grooming behaviors: front-leg rubbing is usually associated with a non-zero phase (a lag) wheres the head-cleaning more often than not has a zero lag (legs moving in-phase).

Frequencies are computed from the AV signal as well. We use numpy.fft.fft() function with the time window of 25 frames (0.25 seconds) and the input size of 160 frames (the

length of the signal with the zero-padding) to compute the spectrum. The frequency at which the spectral power is maximal, is taken as the frequency of the signal.

Segmentation

Our analysis is focused on individual leg movements during grooming. These include contractions and extensions of the front-leg joints. For this purpose we separate the continuous features into segments corresponding to these movements.

The segmentation is performed by applying a stationary threshold to the angular velocity (AV) of the proximal joint angles. These joints determine the whole leg movements (flexions and extensions) so we consider them suitable for the purpose of segmentation. Next, for each segment we compute the averages, minima, and maxima of each continuous feature within that segment. We also compute the duration of each segment as an additional feature. These *segmented features* are used for behavioral classification and for further analysis, including comparing different groups of flies.

Classification of behavior and dimensionality reduction

We collect segments (segment features) from data-sets of groups of flies and pool them together for the purpose of classification. (e.g., experimental and control data-sets are used together.) Altogether we use 63 segment features, including averages of: euclidean distances, AVs, phases between joint pairs, frequencies of all joints, whole-body velocity, segment durations. We also include the maxima of the six AVs, and we can include combined features too (here we only use one combined feature – AV*segment duration).

For better mapping and classification of segments, we account for the temporal context of a segment: for each segment's set of features, we add the same type of features of the next two segments (in time). Thus we analyze features of triplets of segments rather than single segments.

The feature matrix X of the size f x t , where t is the total number of segments and f is the number of segment features multiplied by 3 (to account for the temporal context), is the input to the UMAP dimensionality reduction algorithm.

We use UMAP from https://pypi.org/project/umap-learn/ with the following parameters:

```
n_neighbors=350,
min_dist=0.1,
n_components=2
```

The **X** is thus projected onto two dimensions. For the UMAP construction we can remove some of the data from **X**. Namely, we can remove the data-points (segments) where angular velocity of proximal joints is below a certain value (fly is presumably not moving) or when the quality of data is too low (see quality control).

For the classification we apply the agglomerative clustering onto the 2D UMAP projection. We use AgglomerativeClustering() from sklearn.cluster (https://scikit-learn.org/stable/modules/clustering.html#hierarchical-clustering). We select the number of clusters of 12-14. Thus, we produce 12-14 class labels that can be applied to the 63 features of the segment feature matrix **X**.

Now we can compare the different behavioral classes, across the 63 features, between various groups of flies.

Comparing groups of flies

With 12-14 behavioral classes and 63 features we can now compare different experimental groups of flies to assess the behavioral effects of the experimental procedures. For each *class-feature pair* we can determine whether there is a significant difference between the groups.

With 14 classes and 63 features, there are 882 possible hypotheses to be tested. This calls for the multiple hypotheses adjustment. We applied the Bonferroni method, using the statsmodels.stats.multitest.multipletests() function (https://www.statsmodels.org/dev/generated/statsmodels.stats.multitest.multipletests.html). The alpha parameter was set to 0.05, and the method parameter was set to bonferroni. The t-test was performed using the scipy.stats.ttest_ind()function.

Model

The 13A circuits

The model of 13A and associated circuits was build from simple linear neuronal networks. We did not model individual neurons but rather abstracted them to nodes, interconnected by synaptic weights corresponding to the numbers of synapses obtained from the connectome analysis. Since, the 13A circuits in the right and left front leg neuropil are mirrored and there are slightly more connections on the left side (Figure 2—figure supplement 2), the synaptic weights of the same circuits on the left neuropil were used for modeling purposes.

The network is shown in Figure 6A. Below is the description of the 13A circuit model for one leg. The full model consists of two (front) legs, build the same way.

The two 13A nodes connect to each other reciprocally (inhibitory synapses). The adjacency matrix for these nodes is:

$$W_{13A\leftarrow\rightarrow 13A} = \begin{bmatrix} 0 & -559 \\ -488 & 0 \end{bmatrix}$$

The activation levels of the 13As are simply:

$$A_{13A}^{t+1} = A_{13A}^{t} + W_{13A\leftarrow\rightarrow 13A}^{T} * A_{13A}^{t} - \Theta_{13A}$$

$\mathbf{A}_{13A}$ is a vector of activation levels of the 13As, and $\boldsymbol{\theta}_{13A}$ is a vector of thresholds of 13A neurons.

The 13A nodes inhibit the six motor neurons (MNs). These connections are represented by adjacency matrix:

$$W_{13A\rightarrow MN} = \begin{bmatrix} -1594.0 & -1525.0 & -1525.0 & 0.0 & 0.0 & 0.0 \\ 0.0 & 0.0 & 0.0 & -1525.0 & -1594.0 & -1594.0 \end{bmatrix}$$

The six MNs act on the three pairs of “antagonistic muscles”, which in turn control the changes of joint angles (three per leg). Flexion and extension rates of the antagonistic muscles are directly proportional to the activation levels of the MNs.

The activation levels of the MNs are:

$$A_{MN}^{t+1} = A_{MN}^{t} + W_{13A\rightarrow MN}^{T} * A_{13A}^{t} - \Theta_{MN}$$

$\mathbf{A}_{MN}$ is a vector of activation levels of the MNs, $\mathbf{A}_{13A}$ is a vector of activation levels of 13As, and $\boldsymbol{\theta}_{MN}$ is a vector of thresholds of 13A neurons.

The inputs to the six sensory neurons (SNs) are directly proportional to the flexion and extension rates of the joint muscles. So, the activation levels of the SNs are:

$$A_{SN}^{t+1} = A_{SN}^{t} + extension/flexionrate - \Theta_{SN},$$

where $\mathbf{A}_{SN}$ is a vector of activation levels of SNs, and $\boldsymbol{\theta}_{SN}$ is a vector of thresholds of SNs.

The SNs then feed back onto both, the MNs and the 13As. The adjacency matrix representing the sensory feedback to the MNs is:

$$W_{SN\rightarrow MN} = \begin{bmatrix} 0.0 & 0.0 & 0.0 & 244.0 & 244.0 & 244.0 \\ 0.0 & 0.0 & 0.0 & 244.0 & 244.0 & 244.0 \\ 0.0 & 0.0 & 0.0 & 244.0 & 244.0 & 244.0 \\ 548.0 & 548.0 & 548.0 & 0.0 & 0.0 & 0.0 \\ 548.0 & 548.0 & 548.0 & 0.0 & 0.0 & 0.0 \\ 548.0 & 548.0 & 548.0 & 0.0 & 0.0 & 0.0 \end{bmatrix}$$

The activation levels of the MNs are then updated as follows:

$$A_{MN}^{t+1} = A_{MN}^{t} + W_{SN\rightarrow MN}^{T} * A_{SN}^{t} - \Theta_{MN}$$

where $\mathbf{A}_{MN}$ is a vector of activation levels of MNs, and $\boldsymbol{\theta}_{MN}$ is a vector of thresholds of MNs.

The adjacency matrix representing the sensory feedback to the 13As is:

$$W_{SN\rightarrow 13A} = \begin{bmatrix} 526.0 & 0.0 \\ 526.0 & 0.0 \\ 526.0 & 0.0 \\ 153.0 & 48.0 \\ 153.0 & 48.0 \\ 153.0 & 48.0 \end{bmatrix}$$

And the $\mathbf{A}_{13A}$ activation levels are updated:

$$A_{13A}^{t+1} = A_{13A}^{t} + W_{SN\rightarrow 13A}^{T} * A_{SN}^{t}$$

Activation levels are constrained as follows:

- max($\mathbf{A}_{13A}$) = 2500
- max($\mathbf{A}_{MN}$;$\mathbf{A}_{SN}$) = 200

Minimal activation levels for all neurons are set at zero (so, no negative rates).

Two 13B nodes were added to inhibit the two 13A nodes. The initial weights of the 13B --> 13A were -413 and -160.

Normalization of weight matrices

The synaptic weights are normalized so that they range between -1 and 1. This is done by dividing the **W** matrices by the maximum weight value. We could have used a single weight matrix for the entire 13A network, and divide the weights by the maximum of that "global" matrix. But, this would add an unnecessary constraint to the model, as explained below:

Our objective is to preserve the *rations* between the synaptic weights projecting from the same type of neurons, e.g. all the weights of the projections from the 13A neurons should have the same ratios across both, the $\mathbf{W}_{13A\leftarrow\rightarrow 13A}$ and the $\mathbf{W}_{13A\text{-->}MN}$ matrices. However, weight ratios do not need to be preserved between matrices of *different types*

of projecting neurons, e.g. between the $\mathbf{W}_{13A\text{-->}MN}$ and $\mathbf{W}_{SN\text{-->}MN}$ matrices. This is because the empirically obtained weights (defined as the numbers of synapses) of one neural type do not necessarily correspond to the same quantity obtained from a different type of a neuron, e.g. 6 synapses from 13A to MNs (model weight = 6) do not necessarily correspond to 6 synapses from SNs to MNs (model weight = 6), therefore the ratio of 6 to 6 (1:1) does not need to be preserved. This is why we model each type of neurons by a separate set of weight matrices, corresponding to empirically obtained weights (as shown above) rather than by a single matrix. We normalize the matrices accordingly.

The excitatory network

The model network also needs an excitatory input. Because we do not know the upstream excitatory connections from the connectome we created a “black box” network that takes the simulated dust distribution as the input, and it outputs excitatory signal to the 13A, 13B, and MNs. The “black box” excitatory network consists of a recurrent neural network (RNN) as the hidden layer, with linear synapses and initially random wights.

The hidden RNN layer has 40 nodes. The input layer is the dust grid and the pixel values are its the inputs. The output layer has 21 nodes connecting to the two 13B nodes, the two 12A nodes, and the 6 MN nodes, *per one leg* (so 10 outputs per leg). The same excitatory network also feeds to the other leg’s 13A network, in the same manner. The remaining output node does not project anywhere (it is placed there for future model development where it could output the amplitude of exploratory noise injected into the 13A network).

The agent and the environment

Our model is composed of neuronal circuits embedded in a simple agent that acts on its environment. The agent has two 2D legs, corresponding to the two front legs of a fly, each of which is made of three points (“joints”): proximal, medial, and distal. The distal point (the one farthest from the “body”) can remove the “dust” from the environment. The movement of the “joints” (per leg) is controlled by three pairs of “antagonistic muscles” affecting the three angles formed by the “joints.” Figure 6I shows a frame of a movie where the legs are represented by the three points each.

The environment is composed of a Gaussian distribution of “dust” around the agent (green pixels in Figure 6I). The means of the Gaussian are at the center of the 32 by 32 pixel grid (also the position of the “root” of the front legs), so x=0; y=0. The variance = 5 pixels, in both directions. The maximal amount of dust (at the peak of the Gaussian) is 1.0 (0.99).

The agent can remove the “dust” when the distal “joint” sweeps over the environment with the minimum velocity of 1 pixel/frame. (So, if the “joint” just stays at a given position, the dust is not getting removed. It has to move over it.)

As the grooming behavior is being performed, the “dust” accumulates on the legs, reducing their ability to continue removing it from the grid (the “body”). The “leg cleaning” - removal of the accumulated dust occurs when the two legs are in proximity to each other (Euclidean distance < 5 pixels). The “leg cleaning” rate of dust removal from legs is the same as the body dust removal rate: 0.5/frame.

The three angles (per leg) are constrained. Distal and medial angles: 100° - 180°; proximal angle: 80° -120°.

The fine-tuning of the synaptic weights

When we run the model with the default synaptic weights (see previous sections) nothing happens, i.e. the activation levels either saturate (reach the ceiling values shown above) or fall to zero. The legs of the agent may move once and then the model “freezes.” One way of getting around this problem would be to add a “CPG component” to the model, to drive the periodic excitatory inputs, thereby creating a baseline periodic activity and movements. We could then study the effects of the 13A circuitry on these movements. However, we wanted to see if the model network could generate periodic movements all by itself.

The model weights used are approximate and we do not know the exact ratios between individual modeled weights (the assumption is that the number of biological synapses corresponds to the weights). So, we allow the modeled weights to vary (in value, but not in sign) and yet preserve the approximate ratios obtained from the empirical data. In other words, we are exploring a space of possible models that adhere to approximately the weight ratios obtained empirically. The weights are allowed to vary +/- 20% and cannot change the sign – i.e. inhibitory neurons must remain inhibitory. (In future versions we may decrease this space of exploration to adhere even more closely to the empirical estimates. Conversely, we may increase the exploration space and observe all solutions to see how close our empirical estimates are to the global optimum.)

To explore the space around our empirically estimated weights, we employed a genetic algorithm (GA). We used the PyGAD library (https://pygad.readthedocs.io/en/latest/index.html). Every time the model runs, the agent removes some “dust.” As a fitness function we therefore used the total amount of dust removed over time (500 frames). With that, we set the hyper-parameters of the GA as follows:

num_generations = 150 (this can vary)
num_parents_mating = 20
sol_per_pop = 100 (number of individuals)
num_genes = *n* (*n* is the total number of parameters, i.e. the number of all synaptic weights in the model, including the RNN excitatory “black box” component.
parent_selection_type = "sss"
keep_parents = 1

```
crossover_type = "single_point"
mutation_type = "random"
mutation_probability = 0.1
```

After 150 generations (in case of the model described here, but we often vary that) we arrive to a model solution that can efficiently remove the “dust”, but often just with one leg (i.e. from one side). To speed up the evolutionary process, we then copy all the genes of the 13A network side that removed more dust and paste it to the other side (to the other leg). At this point the legs can remove the dust from both sides, but are too uncoordinated to meet each other, in order to remove the dust from the legs too. Therefore, we run the solution through the GA again (same hyper-parameters). The final fine-tuned model can easily coordinate the legs, ensuring that the “leg rubbing” behavior occurs.

The final weights of the fine-tuned model are within the 80% range of the empirically determined weights (all signs are preserved), as described above. Figure 6B and C shows both sets of weights.

Connectome analysis

Neuronal reconstruction, lineage identification and detection of neuronal partners

We used serial-section transmission electron microscopy (TEM) dataset of female adult *Drosophila* (FANC)[15] to reconstruct 13A and 13B hemilineages in the VNC. These neurons were identified in the EM volume based on their cell body clusters, arborization pattern and nerve bundle entry positions into the ventral neuropil[18,19,66] and comparison with light-level images and axonal tracts labeled with anti-Neuroglian.

13A neurons cluster together and enter the VNC neuropil anteriorly through the ventrolateral position[18,19,66,71]. 13B neurons have contralateral cell bodies and ipsilateral projections, with their axons entering the neuropil through the extreme ventral bundle[18,19,66]. Using confocal microscopy images of 13A and 13B neurons marked with GFP and axonal tracts labeled with anti-Neuroglian for reference comparison, we located these neurons in the EM volume. We manually traced the main neural skeletons and later proof-read automatic segmentations. Then neuronal IDs and cell body coordinates of each 13A and 13B neurons is shown in Table S1.

Manual reconstructions of some of the 13A and 13B neurons were initially performed in CATMAID[113]. Traced skeletons were then imported from CATMAID to Neuroglancer[114]. We identified other 13A neurons and 13B neurons in the corresponding hemilineage bundles and proofread errors in the automated neuronal reconstructions[11]. We fully proofread 62 13A neurons (Table S1), 64 13B neurons in the right prothoracic segment (T1) of VNC, and 25/64 13B neurons in the left T1. We used the automated synapse detection to identify the downstream and upstream connections[11,16]. We used various FANC packages[11] generously available to the community to generate upstream and

downstream partner summary of all the 13A and 13B neurons in R studio (https://rdrr.io/github/flyconnectome/fanc/man/fanc_partner_summary.html).

Connectivity matrix

To plot connectivity matrices between groups of neurons, we utilized Python libraries including pandas, networkx, and matplotlib. We created a directed graph using networkx to represent the connections, where presynaptic and postsynaptic neurons were added as nodes. The thickness and color of edges between nodes were determined by the strength of the connections, and the type of presynaptic or postsynaptic neurons, respectively. Node colors were assigned based on the type of neurons, with specific colors denoting different subtypes of 13A/B neurons and MNs. Finally, we generated the visualization using matplotlib. 13B to 13A connections were manually added in Figure 3B. Leg schematic and MN to muscle connections were also manually added in Adobe Illustrator.

Cosine similarity matrix

We computed the cosine similarity matrix of 13A neurons based on their downstream motor connections in Python using the cosine_similarity from sklearn.metrics.pairwise for computing cosine similarities. A pivot table was created from the DataFrame, with neurons as rows (index) and their post-synaptic targets (post_id) as columns. The values in this table represented the weights of the connections. Duplicates were aggregated using the sum function, and missing values were filled with zeros. The cosine similarity between each pair of neurons was calculated using the cosine_similarity function. Cosine similarity is a measure that calculates the cosine of the angle between two vectors. In this context, each neuron is represented as a vector of its connectivity weights to downstream MNs. The cosine similarity value ranges from -1 to 1, where: 1 indicates that the vectors are identical. 0 indicates that the vectors are orthogonal (no similarity). -1 indicates that the vectors are diametrically opposed. This calculation resulted in a similarity matrix, where each entry (i, j) represents the cosine similarity between the connectivity profiles of neuron i and neuron j. This calculation resulted in a similarity matrix, where each entry (i, j) represents the cosine similarity between the connectivity profiles of neuron i and neuron j. The resulting cosine similarity matrix was visualized using matplotlib. The matrix was displayed as a heatmap with a color gradient indicating the degree of similarity.

Classification of 13A and 13B neurons based on morphology

We used NBLAST[17], a computational method to measure pairwise similarity between neurons based on their position and geometry to identify various subclasses within the hemilineages. This classification was based on similarity scores obtained from Ward's hierarchical clustering and included left-right comparisons.

RESOURCES TABLE

REAGENT or RESOURCE	SOURCE	IDENTIFIER
Antibodies		
Chicken polyclonal anti-GFP	Abcam	RRID: AB_300798
Rabbit (Rb) polyclonal anti- GFP	Invitrogen	Cat #A11122; RRID: AB_221569
Mouse (ms) monoclonal anti-Bruchpilot	DSHB	RRID: AB_2314866
ms anti-Neuroglian (BP104)	DSHB	RRID: AB_528402
Mouse polyclonal anti-V5:DyLight 550	AbD Serotec	RRID: AB_2687576
Rabbit polyclonal anti-HA	Cell Signaling Technologies	RRID: AB_1549585
Rat monoclonal anti-FLAG	Novus Bio	RRID: AB_1625982

Goat anti-Chicken Alexa Fluor 488	Invitrogen	RRID:AB_142924
Goat anti-rabbit Alexa Fluor 488	Invitrogen	RRID. AB_143165
Goat anti-mouse Alexa Fluor 568	Invitrogen	RRID: AB_2534072
Goat anti-mouse Alexa Fluor 633	Invitrogen	RRID:AB_2535719
Goat anti-rabbit Alexa Fluor 568	Invitrogen	RRID: AB_143157
Goat anti-rat Alexa Fluor 488	Invitrogen	RRID: AB_2534074
Donkey anti-rat Alexa 647	Jackson ImmunoResearch	RRID: AB_2340694
Chemicals, Peptides, and Recombinant Proteins		
Insect-a-slip	Bio Quip Products	Cat#2871A
Reactive Yellow 86	Organic Dyestuffs Corporation	CAS 61951-86-8
Experimental Models: Organisms/Strains		

R35G04-GAL4-DBD	Bloomington Stock Center (BDSC)	RRID: BDSC_70351
GAD-GAL4-AD	Deng et al., 2019	
GAD-GAL4-DBD	Gift from Haluck Lacin and James Truman	
Dbx-GAL4-AD	Gift from Haluck Lacin and James Truman	
Dbx-GAL4-DBD	Gift from Haluck Lacin and James Truman	
R11C07 AD	BDSC	RRID: BDSC_70533
w[1118]; P{y[+t7.7] w[+mC]=20XUAS-IVS-CsChrimson.mVenus} attP40	BDSC	RRID: BDSC_55135
P{JFRC7-20XUAS-IVS-mCD8::GFP} attp40	BDSC	RRID: BDSC_32194
UAS-GTACR1	Gift from Adam Claridge-Chang	
w[*]; P{y[+t7.7] w[+mC]=UAS-GtACR1.d.EYFP}attP2	BDSC	RRID: BDSC_92983

w[1118] P{y[+t7.7] w[+mC]=R57C10-FLPL} su(Hw)attP8; PBac{y[+mDint2] w[+mC]=10xUAS(FRT.stop)myr::smGdP-HA} VK00005 P{y[+t7.7] w[+mC]=10xUAS(FRT.stop)myr::smGdP-V5-THS-10xUAS(FRT.stop)myr::smGdP-FLAG} su(Hw)attP1(MCFO3)	BDSC	RRID: BDSC_64087
10XUAS-IVS-eGFP-Kir2.1	von Reyn et al., 2014	
Control-GAL4-AD-GAL4-DBD empty Split: BPp65ADZp(attp40); BPZpGDBD(attp2)	BDSC	RRID: BDSC_79603
Software and Algorithms		
DeepLabCut	Mathis et al., 2018	RRID:SCR_021391
Python		RRID:SCR_008394
MATLAB	MathWorks	RRID: SCR_001622
FIJI	Schindelin et al., 2012	RRID:SCR_002285
Adobe illustrator		RRID:SCR_010279

Adobe Photoshop		RRID:SCR_014199
Braincircuits		https://braincircuits.io/app?p=fruitfly_fanc_public
Neuroglancer	Maitin-Shepard et al., 2021	RRID:SCR_015631
fancr	FANC packages	https://github.com/flyconnectome/fancr
neuPrint	Plaza et al., 2022	https://neuprint.janelia.org/
CATMAID	Saalfeld et al., 2009	RRID:SCR_006278
RStudio		RRID:SCR_000432

ACKNOWLEDGEMENTS

We thank UCSB undergraduate members, especially Ethan Zhang, Yarah Meijer, Daniel Perry, Kaya Minami, and Allene Dang for experimental assistance and proofreading neurons. Sara Abraham, E.Z., Y.M., and K.M. contributed to manual behavioral labeling. Gabe Bello, Katelyn Ross, Kelly McDonald, Kai Thomas, Jada Moore, Yash Shah, Jinyi Dong, Mark Lu, Charliene Lien, Sofia Easton, William Jaber, Paige Gambetta, Maya Teitz, Dhruvi Dalwadi, Abdallah Samarah, Jonathan Carranza, Chandni Patel, Hana Nguyen, Inzar Khan, Garima Sehgal, Sydney Mauch, Yida Huang, Liz Kaslewicz, Nina Shenoy, Joseph Perliss, and Lindsay Easter proofread 13A/B neurons and their partners in the EM dataset. Y.M., K.R., M.T., K.M., G.B., Y.S., J.M., L.E. led the EM team, with training provided by Li Guo, David McNeill, Ladann Kiassat, G.B., E.Z., and Y.M.

We thank Wei-Chung Allen Lee, John Tuthill, and Jasper Phelps for access to the FANC connectome, the FANC community for generously sharing resources, and the Janelia and Cambridge groups for the MANC data.

We are grateful to Akinao Nose and Shingo Yoshikawa for manuscript feedback. For fly strains, we thank James Truman, Haluk Lacin, Gerald Rubin, Benjamin White, Adam Claridge-Chang, and the Bloomington Drosophila Stock Center (NIH grant P40OD018537). This work was supported by NSF Career Award IOS-1943276 and NIH grant RF1NS132900.

AUTHOR CONTRIBUTIONS

D.S.S. **:** Conceptualization, Investigation, Methodology, Formal analysis, Writing – original draft, review and editing. P.R. **:** Modeling, Methodology, Software, Formal analysis. J.H.S. **:** Conceptualization, Funding acquisition, Supervision, Writing – review and editing.

DECLARATION OF INTERESTS

The authors declare no competing interests.

REFERENCES

1. Ravbar, P., Zhang, N., & Simpson, J. H. (2021). Behavioral evidence for nested central pattern generator control of *Drosophila* grooming. *eLife, 10*, e71508. https://doi.org/10.7554/eLife.71508
2. Seeds, A. M., Ravbar, P., Chung, P., Hampel, S., Midgley, F. M., Jr, Mensh, B. D., & Simpson, J. H. (2014). A suppression hierarchy among competing motor programs drives sequential grooming in Drosophila. *eLife, 3*, e02951. https://doi.org/10.7554/eLife.02951
3. Hampel, S., McKellar, C. E., Simpson, J. H., & Seeds, A. M. (2017). Simultaneous activation of parallel sensory pathways promotes a grooming sequence in Drosophila. *eLife, 6,* e28804. https://doi.org/10.7554/eLife.28804
4. Zhang, N., Guo, L., & Simpson, J. H. (2020). Spatial Comparisons of Mechanosensory Information Govern the Grooming Sequence in Drosophila. *Current biology : CB*, *30*(18), 3697–3698. https://doi.org/10.1016/j.cub.2020.08.070
5. Zhang, N., & Simpson, J. H. (2022). A pair of commissural command neurons induces Drosophila wing grooming. *iScience, 25*(2), 103792. https://doi.org/10.1016/j.isci.2022.103792
6. Guo, L., Zhang, N., & Simpson, J. H. (2022). Descending neurons coordinate anterior grooming behavior in Drosophila. *Current biology : CB, 32*(4), 823–833.e4. https://doi.org/10.1016/j.cub.2021.12.055

7. Eichler, K., Hampel, S., Alejandro-García, A., Calle-Schuler, S. A., Santana-Cruz, A., Kmecova, L., Blagburn, J. M., Hoopfer, E. D., & Seeds, A. M. (2024). Somatotopic organization among parallel sensory pathways that promote a grooming sequence in Drosophila. *eLife, 12,* RP87602. https://doi.org/10.7554/eLife.87602
8. Yoshikawa, S., Tang, P., & Simpson, J. H. (2024). Mechanosensory and command contributions to the Drosophila grooming sequence. *Current biology : CB, 34*(10), 2066–2076.e3. https://doi.org/10.1016/j.cub.2024.04.003
9. Miller, A. (1950). The internal anatomy and histology of the imago of Drosophila melanogaster. In Biology of Drosophila (ed. M. Demerec), pp.420-531. New York, NY: John Wiley &Sons.
10. Soler, C., Daczewska, M., Da Ponte, J. P., Dastugue, B., & Jagla, K. (2004). Coordinated development of muscles and tendons of the Drosophila leg. *Development, 131*(24), 6041–6051. https://doi.org/10.1242/dev.01527
11. Azevedo, A., Lesser, E., Mark, B., Phelps, J., Elabbady, L., Kuroda, S., Sustar, A., Moussa, A., Kandelwal, A., Dallmann, C.J., et al. (2024). Connectomic reconstruction of a female Drosophila ventral nerve cord. *Nature*, 10.1038/s41586-024-07389-x.; doi: https://doi.org/10.1038/s41586-024-07389-x
12. Azevedo, A.W., Dickinson, E.S., Gurung, P., Venkatasubramanian, L., Mann, R.S., Tuthill, J.C., 2020. A size principle for recruitment of Drosophila leg motor neurons. *eLife 9*, e56754. https://doi.org/10.7554/eLife.56754
13. Baek, M., & Mann, R. S. (2009). Lineage and birth date specify motor neuron targeting and dendritic architecture in adult Drosophila. *The Journal of neuroscience 29*(21), 6904–6916. https://doi.org/10.1523/JNEUROSCI.1585-09.2009
14. Brierley, D. J., Rathore, K., VijayRaghavan, K., & Williams, D. W. (2012). Developmental origins and architecture of Drosophila leg motoneurons. *The Journal of comparative neurology*, *520*(8), 1629–1649. https://doi.org/10.1002/cne.23003
15. Phelps, J.S., Hildebrand, D.G.C., Graham, B.J., Kuan, A.T., Thomas, L.A., Nguyen, T.M., Buhmann, J., Azevedo, A.W., Sustar, A., Agrawal, S., et al. (2021). Reconstruction of motor control circuits in adult Drosophila using automated transmission electron microscopy. *Cell*, *184*(3), 759–774.e18. https://doi.org/10.1016/j.cell.2020.12.013
16. Lesser, E., Azevedo, A. W., Phelps, J. S., Elabbady, L., Cook, A., Syed, D. S., Mark, B., Kuroda, S., Sustar, A., Moussa, A., et al. (2024). Synaptic architecture of leg and wing premotor control networks in *Drosophila. Nature*, 10.1038/s41586-024-07600-z. https://doi.org/10.1038/s41586-024-07600-z
17. Cheong, H.S.J., Eichler, K., Stürner, T., Asinof, S.K., Champion, A.S., Marin, E.C., Oram, T.B., Sumathipala, M., Venkatasubramanian, L., Namiki, S., et al. (2024). Transforming descending input into behavior: The organization of premotor circuits in the Drosophila Male Adult Nerve Cord connectome *eLife 13*:RP96084. https://doi.org/10.7554/eLife.96084.1
18. Lacin, H., Chen, H. M., Long, X., Singer, R. H., Lee, T., & Truman, J. W. (2019). Neurotransmitter identity is acquired in a lineage-restricted manner in the *Drosophila* CNS. *eLife, 8*, e43701. https://doi.org/10.7554/eLife.43701

19. Harris, R. M., Pfeiffer, B. D., Rubin, G. M., & Truman, J. W. (2015). Neuron hemilineages provide the functional ground plan for the Drosophila ventral nervous system. *eLife, 4*, e04493. https://doi.org/10.7554/eLife.04493
20. Gowda, S. B. M., Banu, A., Hussain, S., & Mohammad, F. (2024). Neuronal mechanisms regulating locomotion in adult Drosophila. *Journal of neuroscience research*, *102*(4), e25332. https://doi.org/10.1002/jnr.25332
21. Mendes, C. S., Bartos, I., Akay, T., Márka, S., & Mann, R. S. (2013). Quantification of gait parameters in freely walking wild type and sensory deprived Drosophila melanogaster. *eLife*, *2*, e00231. https://doi.org/10.7554/eLife.00231
22. Tuthill, J. C., & Azim, E. (2018). Proprioception. *Current biology : CB*, *28*(5), R194–R203. https://doi.org/10.1016/j.cub.2018.01.064
23. Chockley, A. S., Dinges, G. F., Di Cristina, G., Ratican, S., Bockemühl, T., & Büschges, A. (2022). Subsets of leg proprioceptors influence leg kinematics but not interleg coordination in Drosophila melanogaster walking. *The Journal of experimental biology*, *225*(20), jeb244245. https://doi.org/10.1242/jeb.244245
24. Lee S.J. , Dallmann C.J. , Cook A., Tuthill J.C. , Agrawal S. (2024). Divergent neural circuits for proprioceptive and exteroceptive sensing of the *Drosophila* leg. *bioRxiv* 2024.04.23.590808; doi: https://doi.org/10.1101/2024.04.23.590808
25. Bernstein N. (1967). The co-ordination and regulation of movements. *Oxford: Pergamon*
26. Bizzi, E., and Cheung, V. C. (2013). The neural origin of muscle synergies. *Frontiers in computational neuroscience*, *7*, 51. https://doi.org/10.3389/fncom.2013.00051
27. Sherrington C. S. (1892). Notes on the Arrangement of some Motor Fibres in the Lumbo-Sacral Plexus. *The Journal of physiology*, *13*(6), 621–772.17. https://doi.org/10.1113/jphysiol.1892.sp000428
28. Sharrard W. J. (1964). The segmental innervation of the lower limb muscles in man. *Annals of the Royal College of Surgeons of England*, *35*(2), 106–122.
29. Ferrier D. and Yeo G. F. (1881). The functional relations of the motor roots of the brachial and lumbo-sacral plexuses. *Proceedings of the Royal Society of London*, vol. 32, no. 212-215.
30. Bizzi, E., Mussa-Ivaldi, F. A., & Giszter, S. (1991). Computations underlying the execution of movement: a biological perspective. *Science*, *253*(5017), 287–291. https://doi.org/10.1126/science.1857964
31. Giszter, S. F., Mussa-Ivaldi, F. A., & Bizzi, E. (1993). Convergent force fields organized in the frog's spinal cord. *The Journal of neuroscience : the official journal of the Society for Neuroscience*, *13*(2), 467–491. https://doi.org/10.1523/JNEUROSCI.13-02-00467.1993
32. Lemay, M. A., & Grill, W. M. (2004). Modularity of motor output evoked by intraspinal microstimulation in cats. *Journal of neurophysiology*, *91*(1), 502–514. https://doi.org/10.1152/jn.00235.2003
33. Tresch, M. C., & Bizzi, E. (1999). Responses to spinal microstimulation in the chronically spinalized rat and their relationship to spinal systems activated by low threshold cutaneous stimulation. *Experimental brain research*, *129*(3), 401–416. https://doi.org/10.1007/s002210050908

34. Mussa-Ivaldi, F. A., Giszter, S. F., & Bizzi, E. (1994). Linear combinations of primitives in vertebrate motor control. *Proceedings of the National Academy of Sciences*, *91*(16), 7534–7538. https://doi.org/10.1073/pnas.91.16.7534
35. Kargo, W. J., & Giszter, S. F. (2000). Rapid correction of aimed movements by summation of force-field primitives. *The Journal of neuroscience*, *20*(1), 409–426. https://doi.org/10.1523/JNEUROSCI.20-01-00409.2000
36. Lemay, M. A., Galagan, J. E., Hogan, N., & Bizzi, E. (2001). Modulation and vectorial summation of the spinalized frog's hindlimb end-point force produced by intraspinal electrical stimulation of the cord. *IEEE transactions on neural systems and rehabilitation engineering 9*(1), 12–23. https://doi.org/10.1109/7333.918272
37. Maier, M. A., & Hepp-Reymond, M. C. (1995). EMG activation patterns during force production in precision grip. II. Muscular synergies in the spatial and temporal domain. *Experimental brain research*, *103*(1), 123–136. https://doi.org/10.1007/BF00241970
38. Huesler, E. J., Maier, M. A., & Hepp-Reymond, M. C. (2000). EMG activation patterns during force production in precision grip. III. Synchronisation of single motor units. *Experimental brain research*, *134*(4), 441–455. https://doi.org/10.1007/s002210000484
39. Ivanenko, Y. P., Grasso, R., Zago, M., Molinari, M., Scivoletto, G., Castellano, V., Macellari, V., & Lacquaniti, F. (2003). Temporal components of the motor patterns expressed by the human spinal cord reflect foot kinematics. *Journal of neurophysiology*, *90*(5), 3555–3565. https://doi.org/10.1152/jn.00223.2003
40. Hart, C. B., & Giszter, S. F. (2004). Modular premotor drives and unit bursts as primitives for frog motor behaviors. *The Journal of neuroscience*, *24*(22), 5269–5282. https://doi.org/10.1523/JNEUROSCI.5626-03.2004
41. Yakovenko, S., Krouchev, N., & Drew, T. (2011). Sequential activation of motor cortical neurons contributes to intralimb coordination during reaching in the cat by modulating muscle synergies. *Journal of neurophysiology*, *105*(1), 388–409. https://doi.org/10.1152/jn.00469.2010
42. Overduin, S. A., d'Avella, A., Carmena, J. M., & Bizzi, E. (2012). Microstimulation activates a handful of muscle synergies. *Neuron*, *76*(6), 1071–1077. https://doi.org/10.1016/j.neuron.2012.10.018
43. Singh, R. E., Iqbal, K., White, G., & Hutchinson, T. E. (2018). A Systematic Review on Muscle Synergies: From Building Blocks of Motor Behavior to a Neurorehabilitation Tool. *Applied bionics and biomechanics*, *2018*, 3615368. https://doi.org/10.1155/2018/3615368
44. Tresch, M. C., Cheung, V. C., & d'Avella, A. (2006). Matrix factorization algorithms for the identification of muscle synergies: evaluation on simulated and experimental data sets. *Journal of neurophysiology*, *95*(4), 2199–2212. https://doi.org/10.1152/jn.00222.2005
45. Kargo, W. J., Ramakrishnan, A., Hart, C. B., Rome, L. C., & Giszter, S. F. (2010). A simple experimentally based model using proprioceptive regulation of motor primitives captures adjusted trajectory formation in spinal frogs. *Journal of neurophysiology*, *103*(1), 573–590. https://doi.org/10.1152/jn.01054.2007

46. Kutch, J. J., & Valero-Cuevas, F. J. (2012). Challenges and new approaches to proving the existence of muscle synergies of neural origin. *PLoS computational biology*, *8*(5), e1002434. https://doi.org/10.1371/journal.pcbi.1002434
47. Alessandro, C., Delis, I., Nori, F., Panzeri, S., & Berret, B. (2013). Muscle synergies in neuroscience and robotics: from input-space to task-space perspectives. *Frontiers in computational neuroscience*, *7*, 43. https://doi.org/10.3389/fncom.2013.00043
48. Capaday, C., & van Vreeswijk, C. (2015). Linear summation of outputs in a balanced network model of motor cortex. *Frontiers in computational neuroscience*, *9*, 63. https://doi.org/10.3389/fncom.2015.00063
49. Spüler, M., Irastorza-Landa, N., Sarasola-Sanz, A., & Ramos-Murguialday, A. (2016). Extracting muscle synergy patterns from EMG data using autoencoders. In Artificial Neural Networks and Machine Learning–ICANN 2016: 25th International Conference on Artificial Neural Networks, Barcelona, Spain, September 6-9, 2016, Proceedings, Part II 25 (pp. 47-54). *Springer International Publishing.*
50. Aoi, S., & Funato, T. (2016). Neuromusculoskeletal models based on the muscle synergy hypothesis for the investigation of adaptive motor control in locomotion via sensory-motor coordination. *Neuroscience research*, *104*, 88–95. https://doi.org/10.1016/j.neures.2015.11.005
51. Afzal, T., Iqbal, K., White, G., & Wright, A. B. (2017). A Method for Locomotion Mode Identification Using Muscle Synergies. *IEEE transactions on neural systems and rehabilitation engineering, 25*(6), 608–617. https://doi.org/10.1109/TNSRE.2016.2585962
52. Romanes G. J. (1951). The motor cell columns of the lumbo-sacral spinal cord of the cat. *The Journal of comparative neurology*, *94*(2), 313–363. https://doi.org/10.1002/cne.900940209
53. Cruce W. L. (1974). The anatomical organization of hindlimb motoneurons in the lumbar spinal cord of the frog, Rana catesbiana. *The Journal of comparative neurology*, *153*(1), 59–76. https://doi.org/10.1002/cne.901530106
54. Tsuchida, T., Ensini, M., Morton, S. B., Baldassare, M., Edlund, T., Jessell, T. M., & Pfaff, S. L. (1994). Topographic organization of embryonic motor neurons defined by expression of LIM homeobox genes. *Cell*, *79*(6), 957–970. https://doi.org/10.1016/0092-8674(94)90027-2
55. Lanuza, G. M., Gosgnach, S., Pierani, A., Jessell, T. M., & Goulding, M. (2004). Genetic identification of spinal interneurons that coordinate left-right locomotor activity necessary for walking movements. *Neuron*, *42*(3), 375–386. https://doi.org/10.1016/s0896-6273(04)00249-1
56. Crone, S. A., Zhong, G., Harris-Warrick, R., & Sharma, K. (2009). In mice lacking V2a interneurons, gait depends on speed of locomotion. *The Journal of neuroscience, 29*(21), 7098–7109. https://doi.org/10.1523/JNEUROSCI.1206-09.2009
57. Bellardita, C., & Kiehn, O. (2015). Phenotypic characterization of speed-associated gait changes in mice reveals modular organization of locomotor networks. *Current biology : CB*, *25*(11), 1426–1436. https://doi.org/10.1016/j.cub.2015.04.005

58. Lemieux, M., Josset, N., Roussel, M., Couraud, S., & Bretzner, F. (2016). Speed-Dependent Modulation of the Locomotor Behavior in Adult Mice Reveals Attractor and Transitional Gaits. *Frontiers in neuroscience*, *10*, 42. https://doi.org/10.3389/fnins.2016.00042
59. Callahan, R. A., Roberts, R., Sengupta, M., Kimura, Y., Higashijima, S. I., & Bagnall, M. W. (2019). Spinal V2b neurons reveal a role for ipsilateral inhibition in speed control. *eLife*, *8*, e47837. https://doi.org/10.7554/eLife.47837
60. Sengupta, M., Daliparthi, V., Roussel, Y., Bui, T. V., & Bagnall, M. W. (2021). Spinal V1 neurons inhibit motor targets locally and sensory targets distally. *Current biology : CB*, *31*(17), 3820–3833.e4. https://doi.org/10.1016/j.cub.2021.06.053
61. Tripodi, M., Stepien, A. E., & Arber, S. (2011). Motor antagonism exposed by spatial segregation and timing of neurogenesis. *Nature*, *479*(7371), 61–66. https://doi.org/10.1038/nature10538
62. Arber, S., & Davis, G. (2011). Developmental neuroscience. *Current opinion in neurobiology*, *21*(1), 1–4. https://doi.org/10.1016/j.conb.2010.12.001
63. Gordon, E. M., Chauvin, R. J., Van, A. N., Rajesh, A., Nielsen, A., Newbold, D. J., Lynch, C. J., Seider, N. A., Krimmel, S. R., Scheidter, K. M., et al., (2023). A somato-cognitive action network alternates with effector regions in motor cortex. *Nature*, *617*(7960), 351–359. https://doi.org/10.1038/s41586-023-05964-2
64. Yang, W., Kanodia, H., & Arber, S. (2023). Structural and functional map for forelimb movement phases between cortex and medulla. *Cell*, *186*(1), 162–177.e18. https://doi.org/10.1016/j.cell.2022.12.009
65. Gowda, S. B. M., Paranjpe, P. D., Reddy, O. V., Thiagarajan, D., Palliyil, S., Reichert, H., & VijayRaghavan, K. (2018). GABAergic inhibition of leg motoneurons is required for normal walking behavior in freely moving *Drosophila*. *Proceedings of the National Academy of Sciences of the United States of America*, *115*(9), E2115–E2124. https://doi.org/10.1073/pnas.1713869115
66. Shepherd, D., Harris, R., Williams, D. W., & Truman, J. W. (2016). Postembryonic lineages of the Drosophila ventral nervous system: Neuroglian expression reveals the adult hemilineage associated fiber tracts in the adult thoracic neuromeres. *The Journal of comparative neurology*, *524*(13), 2677–2695. https://doi.org/10.1002/cne.23988
67. Truman, J. W., Schuppe, H., Shepherd, D., & Williams, D. W. (2004). Developmental architecture of adult-specific lineages in the ventral CNS of Drosophila. *Development*, *131*(20), 5167–5184. https://doi.org/10.1242/dev.01371
68. Birkholz, O., Rickert, C., Nowak, J., Coban, I. C., & Technau, G. M. (2015). Bridging the gap between postembryonic cell lineages and identified embryonic neuroblasts in the ventral nerve cord of Drosophila melanogaster. *Biology open*, *4*(4), 420–434. https://doi.org/10.1242/bio.201411072
69. Lacin, H., & Truman, J. W. (2016). Lineage mapping identifies molecular and architectural similarities between the larval and adult Drosophila central nervous system. *eLife*, *5*, e13399. https://doi.org/10.7554/eLife.13399
70. Marin, E. C., Morris B. J., Stürner T., Champion A.S., Krzeminski D., Badalamente G., Gkantia M., Dunne C. R., Eichler K., Takemura S., et al. (2023). Systematic annotation of a complete adult male Drosophila nerve cord connectome reveals

principles of functional organisation. *bioRxiv* 2023.06.05.543407 doi:10.1101/2023.06.05.543407.

71. Court, R., Namiki, S., Armstrong, J. D., Börner, J., Card, G., Costa, M., Dickinson, M., Duch, C., Korff, W., Mann, R., Merritt, D., Murphey, R. K., Seeds, A. M., Shirangi, T., Simpson, J. H., Truman, J. W., Tuthill, J. C., Williams, D. W., & Shepherd, D. (2020). A Systematic Nomenclature for the Drosophila Ventral Nerve Cord. *Neuron*, *107*(6), 1071–1079.e2. https://doi.org/10.1016/j.neuron.2020.08.005
72. Costa, M., Manton, J. D., Ostrovsky, A. D., Prohaska, S., & Jefferis, G. S. (2016). NBLAST: Rapid, Sensitive Comparison of Neuronal Structure and Construction of Neuron Family Databases. *Neuron*, *91*(2), 293–311. https://doi.org/10.1016/j.neuron.2016.06.012
73. Mamiya, A., Gurung, P., & Tuthill, J. C. (2018). Neural Coding of Leg Proprioception in Drosophila. *Neuron*, *100*(3), 636–650.e6. https://doi.org/10.1016/j.neuron.2018.09.009
74. Agrawal, S., Dickinson, E. S., Sustar, A., Gurung, P., Shepherd, D., Truman, J. W., & Tuthill, J. C. (2020). Central processing of leg proprioception in *Drosophila*. *eLife*, *9*, e60299. https://doi.org/10.7554/eLife.60299
75. Chen, C., Agrawal, S., Mark, B., Mamiya, A., Sustar, A., Phelps, J. S., Lee, W. A., Dickson, B. J., Card, G. M., & Tuthill, J. C. (2021). Functional architecture of neural circuits for leg proprioception in Drosophila. *Current biology : CB*, *31*(23), 5163–5175.e7. https://doi.org/10.1016/j.cub.2021.09.035

76. Mathis, A., Mamidanna, P., Cury, K. M., Abe, T., Murthy, V. N., Mathis, M. W., & Bethge, M. (2018). DeepLabCut: markerless pose estimation of user-defined body parts with deep learning. *Nature neuroscience*, *21*(9), 1281–1289. https://doi.org/10.1038/s41593-018-0209-y
77. Jovanic, T., Schneider-Mizell, C. M., Shao, M., Masson, J. B., Denisov, G., Fetter, R. D., Mensh, B. D., Truman, J. W., Cardona, A., & Zlatic, M. (2016). Competitive Disinhibition Mediates Behavioral Choice and Sequences in Drosophila. *Cell*, *167*(3), 858–870.e19. https://doi.org/10.1016/j.cell.2016.09.009
78. Chevalier, G., & Deniau, J. M. (1990). Disinhibition as a basic process in the expression of striatal functions. *Trends in neurosciences*, *13*(7), 277–280. https://doi.org/10.1016/0166-2236(90)90109-n
79. Mink J. W. (1996). The basal ganglia: focused selection and inhibition of competing motor programs. *Progress in neurobiology*, *50*(4), 381–425. https://doi.org/10.1016/s0301-0082(96)00042-1
80. Grillner, S., Hellgren, J., Ménard, A., Saitoh, K., & Wikström, M. A. (2005). Mechanisms for selection of basic motor programs--roles for the striatum and pallidum. *Trends in neurosciences*, *28*(7), 364–370. https://doi.org/10.1016/j.tins.2005.05.004
81. Benjamin, P. R., Staras, K., & Kemenes, G. (2010). What roles do tonic inhibition and disinhibition play in the control of motor programs?. *Frontiers in behavioral neuroscience*, *4*, 30. https://doi.org/10.3389/fnbeh.2010.00030
82. Zhu J., Boivin J., Garner A., Ning J., Zhao Y. Q., Ohyama T. (2024) Feedback inhibition by a descending GABAergic neuron regulates timing of escape behavior in Drosophila larvae. *eLife 13*:RP93978 https://doi.org/10.7554/eLife.93978.1

83. Benjamin, P. R., Staras, K., & Kemenes, G. (2010). What roles do tonic inhibition and disinhibition play in the control of motor programs?. *Frontiers in behavioral neuroscience*, *4*, 30. https://doi.org/10.3389/fnbeh.2010.00030
84. Zhao, W., Zhou, P., Gong, C., Ouyang, Z., Wang, J., Zheng, N., & Gong, Z. (2019). A disinhibitory mechanism biases Drosophila innate light preference. *Nature communications*, *10*(1), 124. https://doi.org/10.1038/s41467-018-07929-w
85. Manjila, S. B., Kuruvilla, M., Ferveur, J. F., Sane, S. P., & Hasan, G. (2019). Extended Flight Bouts Require Disinhibition from GABAergic Mushroom Body Neurons. *Current biology : CB*, *29*(2), 283–293.e5. https://doi.org/10.1016/j.cub.2018.11.070
86. Kiehn O. (2016). Decoding the organization of spinal circuits that control locomotion. *Nature reviews. Neuroscience*, *17*(4), 224–238. https://doi.org/10.1038/nrn.2016.9
87. Talpalar, A. E., Endo, T., Löw, P., Borgius, L., Hägglund, M., Dougherty, K. J., Ryge, J., Hnasko, T. S., & Kiehn, O. (2011). Identification of minimal neuronal networks involved in flexor-extensor alternation in the mammalian spinal cord. *Neuron*, *71*(6), 1071–1084. https://doi.org/10.1016/j.neuron.2011.07.011
88. Cowley, K. C., & Schmidt, B. J. (1995). Effects of inhibitory amino acid antagonists on reciprocal inhibitory interactions during rhythmic motor activity in the in vitro neonatal rat spinal cord. *Journal of neurophysiology*, *74*(3), 1109–1117. https://doi.org/10.1152/jn.1995.74.3.1109
89. Kjaerulff, O., & Kiehn, O. (1997). Crossed rhythmic synaptic input to motoneurons during selective activation of the contralateral spinal locomotor network. *The Journal of neuroscience,17*(24), 9433–9447. https://doi.org/10.1523/JNEUROSCI.17-24-09433.1997
90. Whelan, P., Bonnot, A., & O'Donovan, M. J. (2000). Properties of rhythmic activity generated by the isolated spinal cord of the neonatal mouse. *Journal of neurophysiology*, *84*(6), 2821–2833. https://doi.org/10.1152/jn.2000.84.6.2821
91. Endo, T., & Kiehn, O. (2008). Asymmetric operation of the locomotor central pattern generator in the neonatal mouse spinal cord. *Journal of neurophysiology*, *100*(6), 3043–3054. https://doi.org/10.1152/jn.90729.2008
92. Zhang, J., Lanuza, G. M., Britz, O., Wang, Z., Siembab, V. C., Zhang, Y., Velasquez, T., Alvarez, F. J., Frank, E., & Goulding, M. (2014). V1 and v2b interneurons secure the alternating flexor-extensor motor activity mice require for limbed locomotion. *Neuron*, *82*(1), 138–150. https://doi.org/10.1016/j.neuron.2014.02.013
93. Dallmann, C. J., Luo, Y., Agrawal, S., Chou, G. M., Cook, A., Brunton, B. W., & Tuthill, J. C. (2024). Presynaptic inhibition selectively suppresses leg proprioception in behaving *Drosophila*. *bioRxiv : the preprint server for biology*, 2023.10.20.563322. https://doi.org/10.1101/2023.10.20.563322
94. Field L. H., Burrows M. (1982). Reflex effects of the femoral chordotonal organ upon leg motor neurones of the Locust. *J Exp Biol.,* 101 (1): 265–285. https://doi.org/10.1242/jeb.101.1.265
95. Sherrington, C. S., (1910), Flexion-reflex of the limb, crossed extension-reflex, and reflex stepping and standing. *The Journal of Physiology*, 40 doi: 10.1113/jphysiol.1910.sp001362

96. Andersson O, Grillner S (1983). Peripheral control of the cat's step cycle. II Entrainment of the central pattern generators for locomotion by sinusoidal hip movements during "fictive locomotion". Acta Physiol Sc. 118:229-239
97. Kriellaars, D. J., Brownstone, R. M., Noga, B. R., & Jordan, L. M. (1994). Mechanical entrainment of fictive locomotion in the decerebrate cat. *Journal of neurophysiology*, *71*(6), 2074–2086. https://doi.org/10.1152/jn.1994.71.6.2074
98. Pearson K. G. (2004). Generating the walking gait: role of sensory feedback. *Progress in brain research*, *143*, 123–129. https://doi.org/10.1016/S0079-6123(03)43012-4
99. Marlot, D., Macron, J. M., & Duron, B. (1987). Inhibitory and excitatory effects on respiration by phrenic nerve afferent stimulation in cats. *Respiration physiology*, *69*(3), 321–333. https://doi.org/10.1016/0034-5687(87)90086-7
100. Jammes, Y., Buchler, B., Delpierre, S., Rasidakis, A., Grimaud, C., & Roussos, C. (1986). Phrenic afferents and their role in inspiratory control. *Journal of applied physiology (Bethesda, Md. : 1985)*, *60*(3), 854–860. https://doi.org/10.1152/jappl.1986.60.3.854
101. Brown, T. G. (1911). The intrinsic factors in the act of progression in the mammal. Proceedings of the Royal Society of London. Series B, containing papers of a biological character, 84(572), 308-319.

102. Brown T. G. (1914). On the nature of the fundamental activity of the nervous centres; together with an analysis of the conditioning of rhythmic activity in progression, and a theory of the evolution of function in the nervous system. *The Journal of physiology*, *48*(1), 18–46. https://doi.org/10.1113/jphysiol.1914.sp001646
103. Stuart, D. G., & Hultborn, H. (2008). Thomas Graham Brown (1882--1965), Anders Lundberg (1920-), and the neural control of stepping. *Brain research reviews*, *59*(1), 74–95. https://doi.org/10.1016/j.brainresrev.2008.06.001
104. Duysens, J., De Groote, F., & Jonkers, I. (2013). The flexion synergy, mother of all synergies and father of new models of gait. *Frontiers in computational neuroscience*, *7*, 14. https://doi.org/10.3389/fncom.2013.00014
105. Zhong, G., Shevtsova, N. A., Rybak, I. A., & Harris-Warrick, R. M. (2012). Neuronal activity in the isolated mouse spinal cord during spontaneous deletions in fictive locomotion: insights into locomotor central pattern generator organization. *The Journal of physiology*, *590*(19), 4735–4759. https://doi.org/10.1113/jphysiol.2012.240895
106. Cowey A. (1979). Cortical maps and visual perception: the Grindley Memorial Lecture. *The Quarterly journal of experimental psychology*, *31*(1), 1–17. https://doi.org/10.1080/14640747908400703
107. Raj, A., & Chen, Y. H. (2011). The wiring economy principle: connectivity determines anatomy in the human brain. *PloS one*, *6*(9), e14832. https://doi.org/10.1371/journal.pone.0014832
108. Pérez-Escudero, A., & de Polavieja, G. G. (2007). Optimally wired subnetwork determines neuroanatomy of Caenorhabditis elegans. *Proceedings of the National Academy of Sciences of the United States of America*, *104*(43), 17180–17185. https://doi.org/10.1073/pnas.0703183104

109. Chklovskii, D. B., Schikorski, T., & Stevens, C. F. (2002). Wiring optimization in cortical circuits. *Neuron*, *34*(3), 341–347. https://doi.org/10.1016/s0896-6273(02)00679-7
110. Lemay, M. A., & Grill, W. M. (2004). Modularity of motor output evoked by intraspinal microstimulation in cats. *Journal of neurophysiology*, *91*(1), 502–514. https://doi.org/10.1152/jn.00235.2003
111. Karashchuk, L., Li, J. S. L., Chou, G. M., Walling-Bell, S., Brunton, S. L., Tuthill, J. C., & Brunton, B. W. (2024). Sensorimotor delays constrain robust locomotion in a 3D kinematic model of fly walking. *bioRxiv*, 2024-04.
112. Jenett, A., Rubin, G. M., Ngo, T. T., Shepherd, D., Murphy, C., Dionne, H., Pfeiffer, B. D., Cavallaro, A., Hall, D., Jeter, J.,et al., (2012). A GAL4-driver line resource for Drosophila neurobiology. *Cell reports*, *2*(4), 991–1001. https://doi.org/10.1016/j.celrep.2012.09.011
113. Ravbar, P., Branson, K., & Simpson, J. H. (2019). An automatic behavior recognition system classifies animal behaviors using movements and their temporal context. *Journal of neuroscience methods*, *326*, 108352. https://doi.org/10.1016/j.jneumeth.2019.108352
114. Saalfeld, S., Cardona, A., Hartenstein, V., & Tomancak, P. (2009). CATMAID: collaborative annotation toolkit for massive amounts of image data. *Bioinformatics*, *25*(15), 1984–1986. https://doi.org/10.1093/bioinformatics/btp266
115. Maitin-Shepard, J. et al. (2021) google/neuroglancer: Zenodo https://doi.org/10.5281/zenodo.5573294